Universitat de les Illes Balears

MASTER'S THESIS

ALFVÉN WAVE HEATING IN PARTIALLY IONISED THIN THREADS OF SOLAR PROMINENCES

Llorenç Melis Sánchez

Master's Degree in Advanced Physics and Applied Mathematics

(Specialisation/Pathway *Astrophysics and Relativity*)

Centre for Postgraduate Studies

Academic Year 2019-20

Key words:

Sun, prominences/filaments, MHD, Alfvén waves, heating

Thesis Supervisor: Roberto José Soler Juan

Abstract

Quiescent solar filaments and prominences are clouds of cool and dense plasma in the solar corona suspended against gravity by forces which are supposed to be of magnetic origin. Prominences are highly dynamic structures that display oscillations that seem to be ubiquitous, as shown in observations. These oscillations are magnetohydrodynamic waves from a wide range of frequencies that are probably driven by motions in the underlying solar photosphere and may transport energy up to prominences suspended in the above corona. Dissipation of wave energy can lead to heating of the cool prominence plasma, thereby contributing to the local energy balance within the prominence.

In this work we analyse the effect of Alfvén wave dissipation as a heating mechanism in thin threads of solar prominences. We consider a 1D prominence thread model with a constant magnetic field, while the density and temperature vary along the thread in a fashion that mimics the observations. We consider Ohm's and ambipolar diffusions and we use two different relations between the temperature and the ionisation degree. We investigate the standing and propagating modes cases using a semi-analytical approach.

The results show that for the standing modes, the damping is almost negligible unless very high harmonics are considered, and the heating produced by the Alfvén wave dissipation does not compensate the radiative cooling. For the propagating modes we have seen that the injected energy flux in the thread has relative minimums for the frequencies that correspond to the eigenfrequencies of the standing modes, which suggests the existence of resonances. For the energy balance, a broadband spectrum of propagating modes provides enough heating at the centre of the thread to compensate the cooling, but wave heating is inefficient in the hot coronal part.

Contents

1 Introduction

1.1 The Sun

The Sun is the most studied star; because is the nearest one. By studying it, we can understand how the stars behave in terms of, for example the internal reactions, magnetic fields or waves. Stars are made mainly of plasma, which is an aggregate state of matter. Plasma is a fluid state similar to a gas but the particles that form the fluid are not neutral. Instead, they are ionised although there can be neutral particles too.

The Sun is a star of spectral type G2V, which implies that it is a star from the main sequence. The composition of the Sun is 74 % hydrogen, 24 % helium and the other 2 % are heavier elements. The main physical properties of the Sun are given in Table 1.

Absolute magnitude	4.8
Age	4.5×10^9 years
Mass, $M_\odot$	1.99×10^{30} kg
Radius, $R_\odot$	6.96×10^8 m
Mean density	$1.4 \times 10^3\,\mathrm{kg\,m^{-3}}$
Mean distance from Earth	1 UA $= 1.5 \times 10^{11}$ m
Surface gravity, $g_\odot$	$274\,\mathrm{m\,s^{-2}}$
Escape speed	$618\,\mathrm{km\,s^{-1}}$
Luminosity, $L_\odot$	3.86×10^{26} W
Equatorial rotation period	26 days
Angular momentum	$1.7 \times 10^{41}\,\mathrm{kg\,m^2\,s^{-1}}$
Mass loss ratio	$1 \times 10^9\,\mathrm{kg\,s^{-1}}$
Effective temperature	5785 K

Table 1: Physical properties of the Sun.

Although at first it was believed that the Sun was a homogeneous cosmical body, in ancient Greece and China astronomers recorded the existence of sunspots, which were observed with the naked eye. However, the systematic observations of the Sun began in the 17th century, when Galileo Galilei used the telescope to observe sunspots. Nowadays we know that most of the observed solar structures are caused by the activity of the solar magnetic field [32].

Internal structure of the Sun

The interior of the Sun is divided into 3 parts: the core, the radiative zone and the convective zone. The opacity of the interior of the Sun is so big that it can not be observed and we can only see the surface. A schematic representation of the solar interior is seen in Figure 1.

The core is the central part of the Sun. It covers 20 % of the radius and has a mean temperature and density of 1.5×10^7 K and $1.6 \times 10^5\,\mathrm{kg\,m^{-3}}$ respectively. These values are large enough to produce nuclear reactions. The core has half the mass of the Sun but produces 99 % of the Sun's energy. This is where helium atoms are formed. These atoms are formed generally with the p-p cycle but they can also be produced with CNO cycles.

The radiative zone is located between 25 % and 70 % of the Sun radius. In this zone the temperature and the density vary between 2×10^6 and 7×10^6 K and 200 and $2 \times 10^4\,\mathrm{kg\,m^{-3}}$ respectively. In this region light is transported form the core to the convective zone very slowly, since the high density of matter in this region means a photon can not travel too far without

encountering another particle, causing it to change direction (scattering) and to lose some energy in the process. The very high opacity implies that a photon takes 10^7 years to reach the solar surface.

The convective zone is the outermost region of the solar interior. In this zone the temperature gradient is too high to remain in hydrostatic equilibrium. It is a thick layer of 2×10^5 km that transports energy from the edge of the radiative zone to the surface through giant convection cells. The plasma at the bottom of the convective zone is extremely hot and bubbles to the surface where it loses its heat to space. Then the plasma cools down and returns to the bottom of the convection zone. In this region the temperature and the density change their values a lot, being their values at the surface 5800 K and $8 \times 10^{-5}\,\mathrm{kg\,m^{-3}}$.

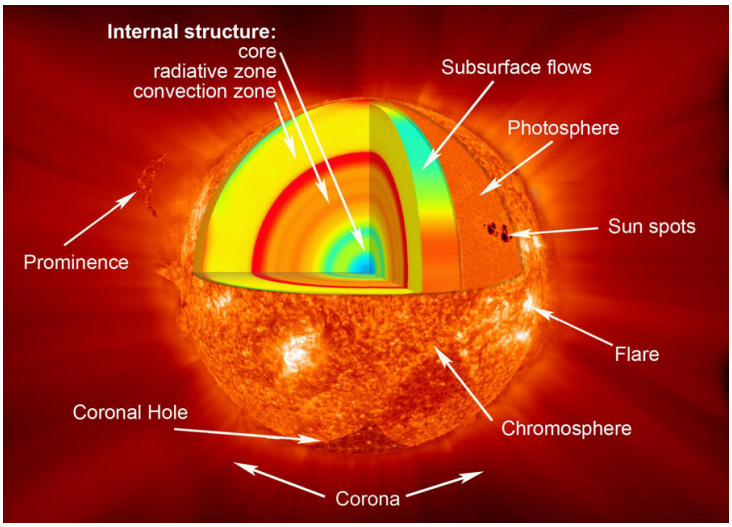

Figure 1: *A schematic representation of the different layers of the Sun.* Credit: SOHO (ESA & SOHO).

Solar atmosphere

The solar atmosphere is divided into three parts: the photosphere, the chromosphere and the corona.

The photosphere is the surface layer of the Sun. This layer is where the Sun becomes opaque. We cannot see the material below this layer. In this region the energy produced at the Sun's interior emerges. This energy takes the form of photons, which have passed the high density layer and can escape the Sun without colliding with another atom or ion. It has a thickness of 100 km. The diameter of the Sun is determined by the diameter of the photosphere. In this region the pressure and the density are much lower than in the interior. The pressure and the density are much lower than those of the atmosphere of the Earth. The main structure of the photosphere is called granulation. These granules are generally 700 to 1000 km in diameter and have a lifetime of 5 to 10 minutes. There are also the supergranules, which are about 35000 km and have a lifetime of 24 hours approximately. The appearance of the granules in observations is like a bright area surrounded by darker and cooler regions. Besides the granulation, the other most important inhabitants of the photosphere are the sunspots: dark and cool regions with intense magnetic fields. The largest sunspots are several times larger than the size of Earth.

On the top of the photosphere there is the chromosphere. This region is about 2000 to 3000 km thick. The mean temperature of the chromosphere is about 10000 K, which means that it

is hotter than the photosphere. This temperature increase does not stop in the chromosphere. There is a transition region where the temperature varies from 10000 K to a million degrees. This region is called the transition region. The dependence of the temperature as a function of height is shown in Figure 2.

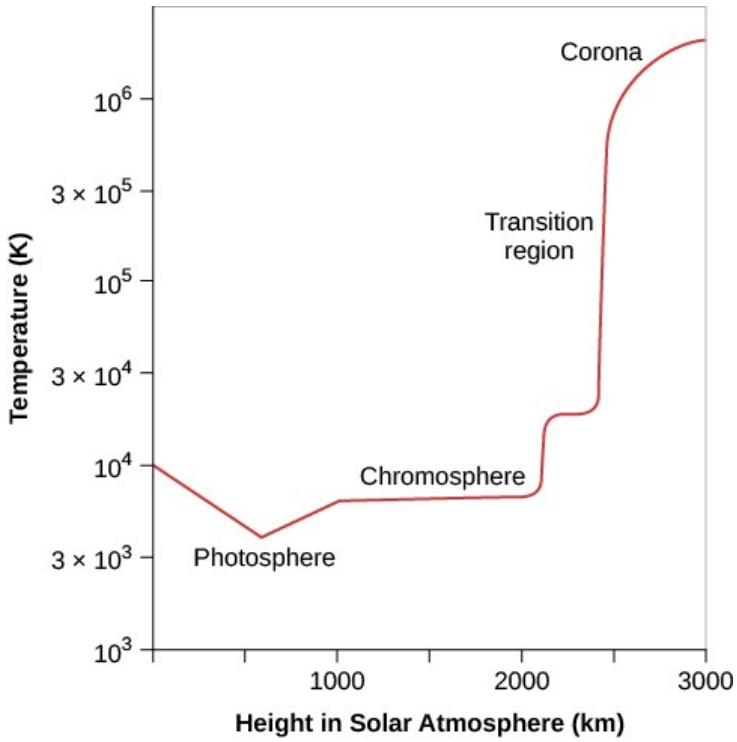

Figure 2: *Temperature in the solar atmosphere as a function of height.* Credit: J. B. H. Baker, "Lecture 8: Solar Activity," in ECE-5146 Space Science I, 15-Sep 2017

The outermost part of the Sun is the corona. This region extends millions of kilometres above the photosphere and emits about half as much light as the full moon. The corona has a very low density, which is about 10^9 atoms per m^3, compared to the 10^{16} atoms per m^3 of the photosphere. In the corona there are important structures such the coronal streamers, which are practically radial structures, or the coronal loops [2].

The Sun's atmosphere produces a stream of charges particles, which is called solar wind. There are two kinds of solar winds, the fast solar wind and the slow solar wind. It is estimated that the Sun loses about 10 million tones of matter every year through this wind, which mainly streams from large and cool regions called coronal holes.

1.2 Prominences and threads

Quiescent solar filaments are clouds of cool and dense plasma in the corona that are suspended against gravity by forces thought to be of magnetic origin. They are formed along the inversion polarity line in or between the weak remnants of magnetically active regions. The first investigations suggested that their fine structure was composed by many horizontal and thin dark threads presumably oriented along the magnetic field [10], [19]. More recent observations using the high-resolution H_α filters have allowed to observe this fine structure with much greater detail [24], [13].

The physical properties of prominences cores are: the electron density has a value between 10^9 to 10^{11} m^{-3}, although recent observations inferred a value of $1 \times 10^{15}\,m^{-3}$ in an active region

filament [26]. The temperature values are in a range between 7500 and 9000 K. The gas pressure of prominence core is in the range 0.02-1 dyne cm^{-2}. The usual value of magnetic field is between 8 to 10 G [31].

Prominences are highly dynamic structures that display flows. These flows have been observed in H_α, UV and EUV lines, and their study and characterisation are of great interest for the understanding of prominence formation and stability, the mass supply and the prominence magnetic field structure. In H_α filter a complex dynamics with vertical downflows and upflows as well horizontal flows is often observed [9]. The velocities are in the range between 2 and 35 km/s, while in the EUV lines these velocities values seem to be higher. This results are related to the difference of temperatures of the lines, so the velocities correspond to different parts of the prominence.

Solar prominences are subject to various types of oscillatory motions. Some of the first works on this subject were concerned with large amplitudes induced by disturbances from a nearby energetic event. Many later observations using ground-based telescopes pointed out that quiescent prominences and filaments display small amplitude oscillations [12]. These oscillations have been interpreted in terms of standing or propagating magnetohydrodynamic (MHD) waves. In MHD the relevant velocities are the Alfvén speed and the sound speed, being their values in quiescent prominences of the order of 100 and 11 km/s respectively. Using this interpretation, a number of theoretical models have been set up in order to try to understand the prominence oscillatory behaviour. The study of prominence oscillations can provide with an alternative approach for probing their internal structure. The magnetic field structure and physical plasma properties are often hard to infer directly and wave properties directly depend on these physical conditions. Therefore, prominence seismology seeks to obtain information about prominence physical conditions from a comparison between observations and theoretical models of oscillations.

Prominence oscillations have been classified according to different measurable quantities: period, oscillatory amplitude, polarisation. In [30] the use of velocity amplitude as the only classification parameter was used. Oscillations are classified into small and large amplitudes, being their amplitudes smaller than 3 km/s and larger than 20 km/s respectively. Although the detection of intermediate values revealed that the velocity amplitude is not enough to identify an oscillatory event, this classification is still used because small and large amplitude oscillations represent different phenomena. Small amplitudes are not related to external disturbances and only affect a small volume of the prominences. Large amplitudes are associated to an energetic event that sets the entire prominence into an oscillatory state. Frequently, large-amplitude oscillations are detected before prominence eruption. The typical size of a prominence is about many thousands of kilometres. The comparison between an erupting prominence and Earth is shown in Figure 3. A schematic diagram of the structure of a prominence with its fibrils is shown in 4.

As said before, the internal structure of prominences is made of fine filaments called threads. An example of how threads are seen using telescopes is Figure 7. The discovering of threads has developed the study of thread oscillations. Based on the observations, there are two different situations: waves propagating along the thread and standing modes that affect the whole thread body. Although both longitudinal and transverse oscillations have been detected, in this work we focus on the transverse oscillations alone. A high-resolution observation of threads is shown in Figure 5.

A simple thread model consists of an infinitely long cylinder filled with cold, dense plasma and embedded in the hooter and less dense corona. The field line curvature is neglected and the magnetic field is uniform and parallel to the cylinder. The MHD modes of this configuration have been extensively studied [11]. The mode of interest is the kink mode, because it is the only one that produces a significant transverse displacement in the thread, which can explain

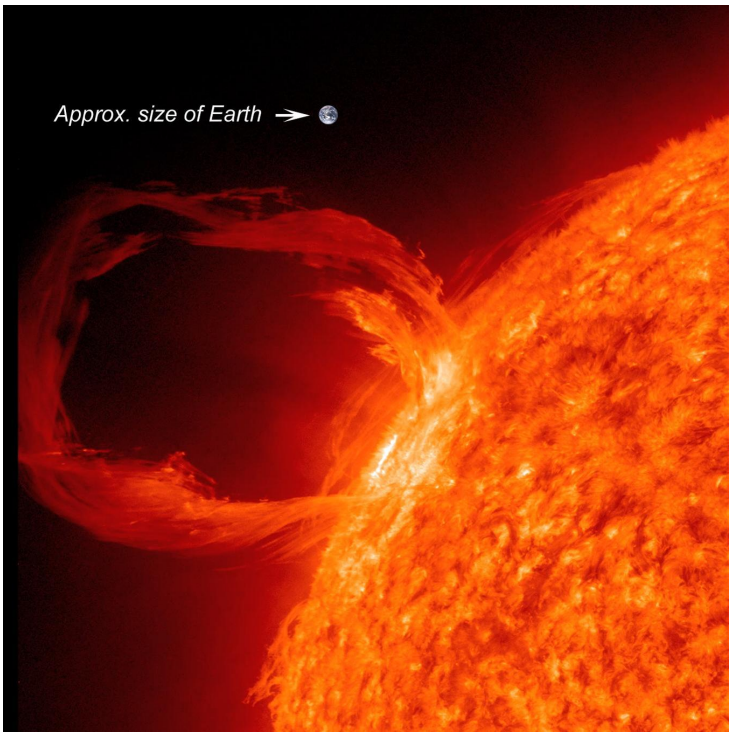

Figure 3: *EUV image of an erupting solar prominence. The size of The Earth is depicted for comparison purposes.* Credit: NASA/SDO.

the observations of transverse oscillations. Considering that the thread radius is much smaller than the wavelength, the kink frequency is given by

$$\omega_k = k_z \sqrt{\frac{\rho_p v_{Ap}^2 + \rho_c v_{Ac}^2}{\rho_p + \rho_c}} = k_z v_{Ap} \sqrt{\frac{2\zeta}{1+\zeta}}, \tag{1.1}$$

where k_z is the wavenumber, ρ_p and ρ_c the thread and coronal densities, ζ the density contrast and $v_{Ap,c}$ the thread and coronal Alfvén velocities. In the case of standing modes, the values of k_z are fixed, discrete and related to the length of the thread. Conversely, in the case of propagating (driven) waves ω_k is fixed to the driver frequency.

An even simpler model to represent a very thin prominence thread is considering a single magnetic field line. In this 1D case, the transverse oscillations are described by Alfvén waves, whose frequency is $\omega_A = k_z v_{Ap}$ in a homogeneous thread. This 1D approach is mathematically simpler and allows the study of the effects introduced by plasma inhomogeneity along the thread, which is much more difficult to study in the cylindrical flux tube model explained above. For this reason, we shall use here a simplified 1D model to represent a filament thread. An example of a single thread structure is shown in Figure 6.

1.3 Observations

The main purpose of studying prominence oscillations is to obtain some insight into their physics using the seismological approach, which has the aim to determine physical parameters that are difficult to measure by direct means in magnetic and plasma structures. The information that observations should provide are the periods, damping time, phase velocity, etc. of these phenomena. Observations should also determine whether these periodic variations are standing oscillations or propagating waves,whether they affect some prominence threads or larger areas of

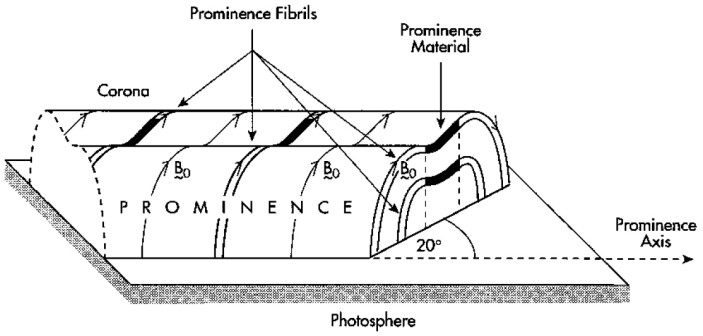

Figure 4: *Schematic diagram of a prominence with its internal structure.* Credit: [17].

a prominence, whether threads oscillate independently from their neighbours or which physical variables are disturbed and by which amount.

In the small oscillations observations several detection methods have been used. The most often method used is the spectroscopic, but also using images in specific spectral lines [39], [24], [16]. The vast majority of spectroscopic reports of prominence oscillations are based on the analysis of Doppler velocity. Other spectral indicators like the line intensity and line width have also been used in the search for periodic variations in prominences.

Prominence oscillations periods have a wide range of values. In the early observations periods ranged from a few minutes, 15-20 minutes [12], [20] to 40-90 minutes [7], [8], [38], [5]. This apparent tendency led to divide the periods into two groups: short- and long-period oscillations, being the short ones below 10 minutes and the long ones in the range of 40-90 minutes. There exists also the intermediate-period oscillations which were detected later [40], [33]. Nowadays very short- and very long-period oscillations have been observed and although the classification is still used, it does not give any information about the origin and nature of the oscillations. Threads of a single prominence can support a wide range of periods: from 50 to 6000 seconds.

The oscillatory amplitude using the Doppler peak method detects peaks that usually range from less than 0.1 km/s to 2-3 km/s, although higher peaks have been observed [8], [27], [28]. The range of the displacement ranges from 19 to 1400 km and the velocity amplitude ranges from 0.2 to 23 km/s, being their predominant value 200 km and 5 km/s respectively [16], [21].

It is observed that the oscillations tend to decrease in time in such a way that the periodicity totally disappears after a few seconds. After fitting the function $v_0 \cos(\omega t + \phi) \exp(-t/\tau)$ to Doppler velocity time series the value of the damping time τ can be derived [27]. The values of τ are usually between 1 to 4 times the corresponding period. The evolution of the velocity in terms of the time in an oscillation observed in a quiescent prominence can be seen in Figure 8.

To derive the wavelength λ and phase speed c_{ph} of oscillations, time signals at different locations on the prominence must be acquired. The signature of a propagating wave is a linear variation of the oscillatory phase with distance. Studying Doppler velocity at different times, wave propagations along the threads were detected, which allowed to compute the wavelength [24], [23]. The phase velocity of the oscillations can be derived from the inclination of the coherent features in the Doppler velocity time-slice diagrams.

1.4 Motivation of this work

In view of the observational evidence that transverse MHD waves and oscillations are damped in prominences, a question arises: is the dissipation of wave energy important for the energy balance in the prominence plasma?

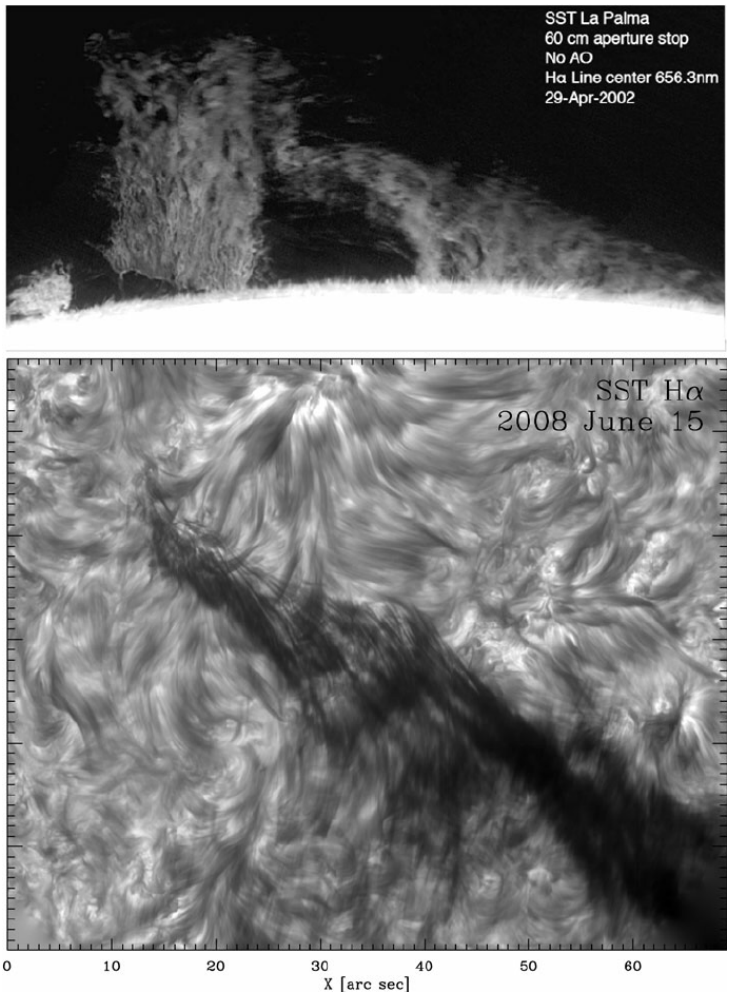

Figure 5: *High resolution observations of threads in a quiet prominence (upper panel) and a quiescent filament (lower panel) using the filter Hα.* Credit: [22].

The aim of this study is to discuss the role of the Alfvén wave dissipation as a heating mechanism in thin threads of solar prominences. We will start by considering a 1D model for a prominence thread and will use two different methods to relate the temperature and the ionisation rate in the thread. On this model we will solve numerically the correspondent system of linearised MHD equations and obtain the velocity and the magnetic field perturbations associated with Alfvén waves. Once we obtained the wave perturbations, we will calculate the heating function. Then we will compare the heating and cooling rate to estimate whether wave heating can compensate some fraction of the energy lost by radiation. We will calculate two different kinds of wave modes: the standing modes and the propagating modes.

In a previous study, [36] investigated Alfvén wave heating in a simple prominence model made of a homogeneous slab embedded in a homogeneous corona. They only studied propagating waves and found that wave heating can compensate for about 10 % of prominence radiative losses. The purpose here is to perform a similar investigation but in this case of a single prominence thread. In addition, plasma non-uniformity along the magnetic field is considered here, while it was ignored in [36]. Moreover, we investigate both standing and propagating waves.

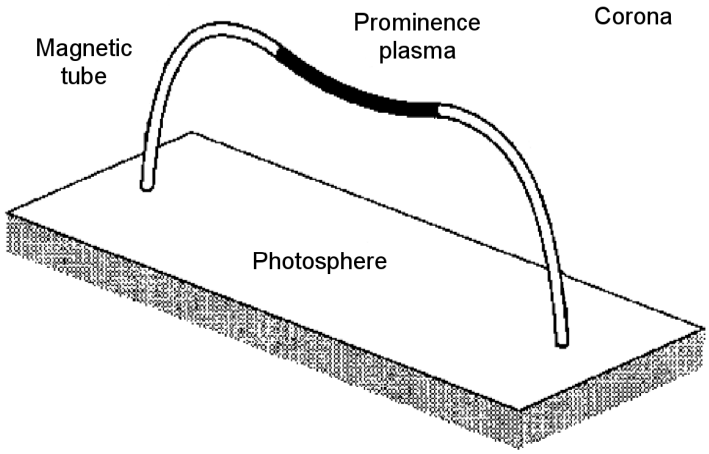

Figure 6: *Structure of a single thread and its surrounding regions.* Credit: [17].

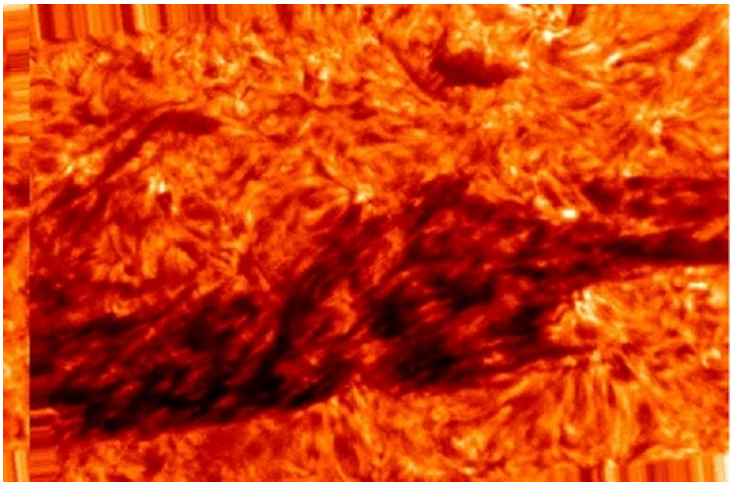

Figure 7: *Prominence threads observed using the H_α line with the Swedish Solar Telescope in La Palma.* Credit: [25].

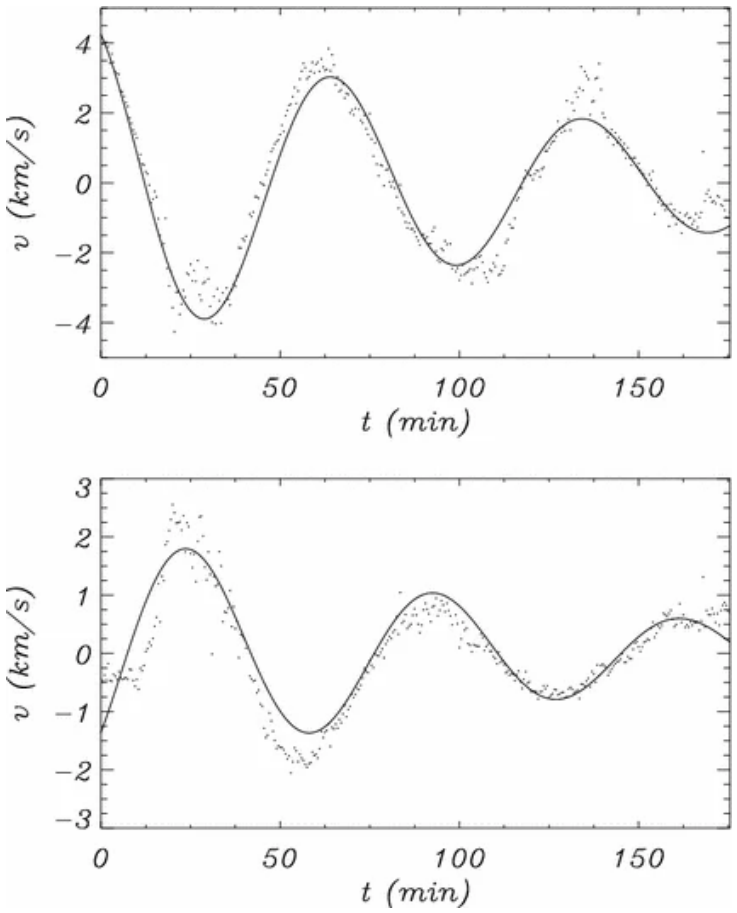

Figure 8: *Observed Doppler velocity (dots) and fitted functions (continuous line) versus time at two different points in a quiescent prominence.* Credit: [1].

2 Model

For this study we consider a 1D prominence thread of length L that is aligned with the z-axis. This thread is centred at $z = 0$ and their ends are at $z = -L/2$ and $z = L/2$.

This model has a constant pressure of value $p = 5 \times 10^{-3}$ Pa and the density varies along z according to a Lorentzian form, that aims to mimic the expected density profile along prominence threads, see [34]

$$\rho(z) = \frac{\rho_0}{1 + 4(\chi - 1)z^2/L^2}, \tag{2.1}$$

where $\rho_0 = 1 \times 10^{-10}\,\mathrm{kg\,m^{-3}}$ is the density at the centre of the thread and $\chi = 100$ is the ratio between the density at $z = 0$ and that at $z = \pm L/2$. The density profile is represented in Figure 9.

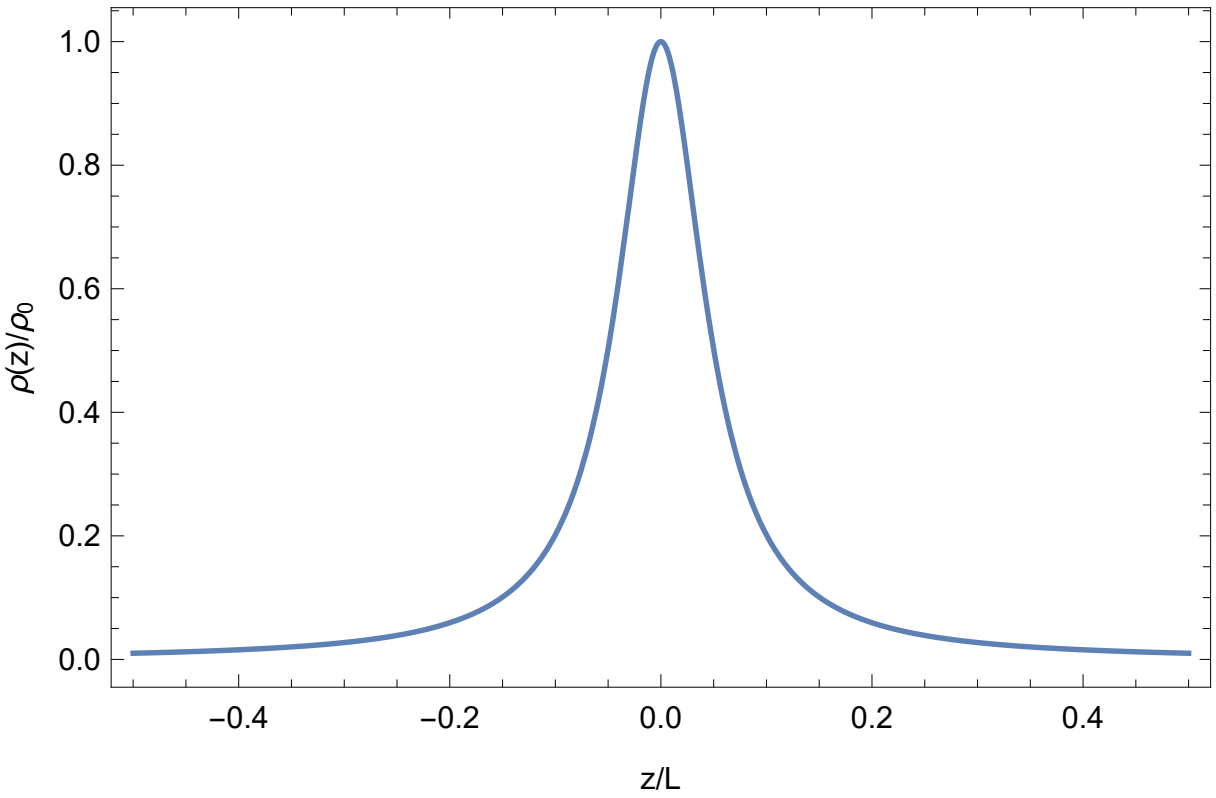

Figure 9: *Density profile along the prominence thread.*

Once we have defined the pressure and the density of the thread, the next step is obtain a profile for the temperature T and the ionisation fraction ξ_i in terms of z. Due to the relatively low temperatures the plasma is only partially ionised, so that $\xi_i \neq 1$. Since ξ_i depends on T, we need two equations to close the system. The first equation we shall use is the equation of state for an ideal gas. The second equation we need is a relation between ξ_i and T that determines the ionisation state. We use two different methods: the first one uses the Saha equation, which assumes local thermodynamic equilibrium (LTE) and the second one uses the relation between the temperature and the ionisation given by [14], which is based on non-LTE radiative transfer computations. One of the purposes of this work is to compare the results obtained for both approaches.

2.1 Saha and Heiznel methods

The Saha equation relates the ionisation rate with the temperature and the pressure under the assumption of LTE. In the case of a hydrogen plasma, the expression of ξ_i according to the Saha equation is

$$\xi_i = \frac{1}{2} M \left(\sqrt{1 + \frac{4}{M}} - 1 \right), \tag{2.2}$$

where

$$M \approx 4 \times 10^{-6} \rho^{-1} T^{3/2} \exp(-T^*/T), \tag{2.3}$$

with $T^* = 1.578 \times 10^{-5}$ K.

For the Heinzel method we use the values of Table 2 in order to relate the temperature and the ionisation. These values are adapted from the numerical results given in [14]. Using these values of T and ξ_i we can interpolate and plot their relation imposing $\xi_i = 1$ (full ionisation) for $T \geq 20000$ K. See Figure 12.

T	6000	8000	10000	12000	14000
ξ_i	0.41	0.52	0.68	0.81	0.89

Table 2: Values of the ionisation ξ_i for various values of the temperature (in K) for a value of the pressure of 5×10^{-3} Pa. Adapted from [14].

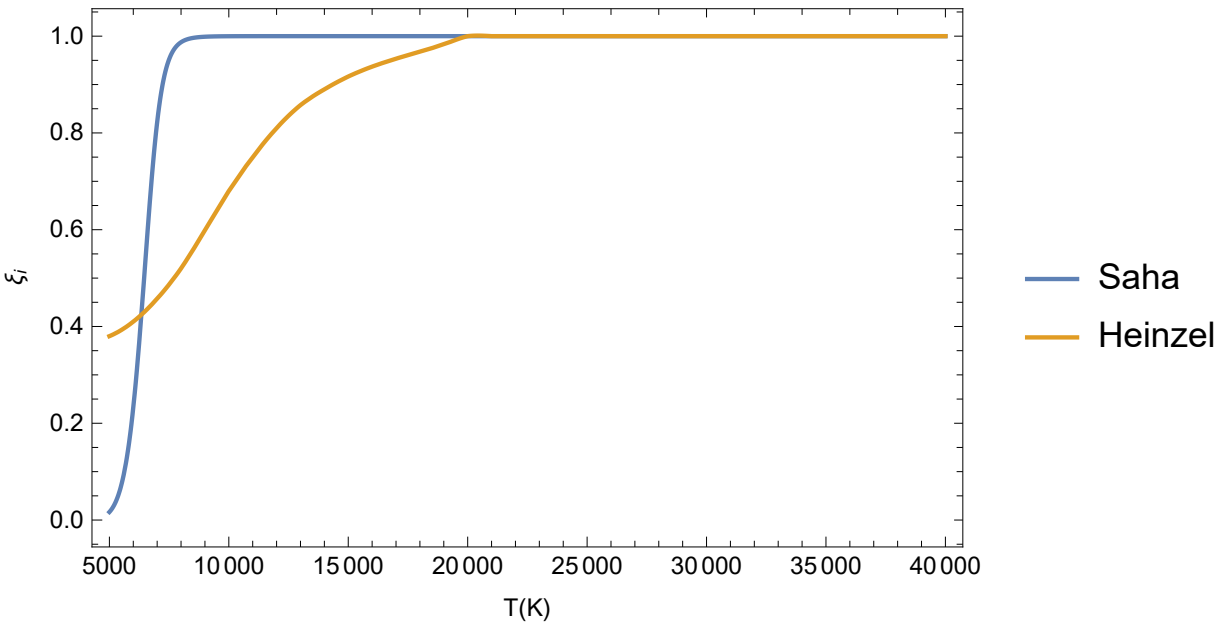

Figure 10: *Ionisation fraction in terms of T for the Heinzel method compared to the Saha equation.*

In Figure 10 we plot the relation between the temperature and the ionisation fraction for the Saha and Heinzel method. Comparing the methods, the ionisation using the Saha method raises the completely ionised state much faster than the Heinzel method when the temperature increases.

2.2 Temperature and ionisation profiles

We calculate the temperature and the ionisation with the ideal gas equation, which is defined as

$$p = (1 + \xi_i)\rho RT, \tag{2.4}$$

where R is the ideal gas constant with a value of 8300 $\mathrm{J\,mol^{-1}\,K^{-1}}$.

In the Saha method we calculate the profiles using Equations (2.4) and (2.2), and in the Heinzel method we use Equation (2.4) with the numerical interpolation of Table 2.

The results for the temperature and the ionisation can be seen in Figures 11 and 12 respectively. For the temperature both methods give a similar result, showing a parabolic-like profile with the minimum at the centre of the thread and the maximum at the ends. The central temperature is around 5000 K and the temperature at the ends is around 300000 K. For the ionisation the Saha method gives a narrower partially ionised region but the minimum value is much lower than that provided by Heinzel method, for which there is a wider partially ionised region but the minimum ionisation rate is larger. The ionisation fraction at the centre is 0.095 for the Saha method and 0.372 for the Heinzel method.

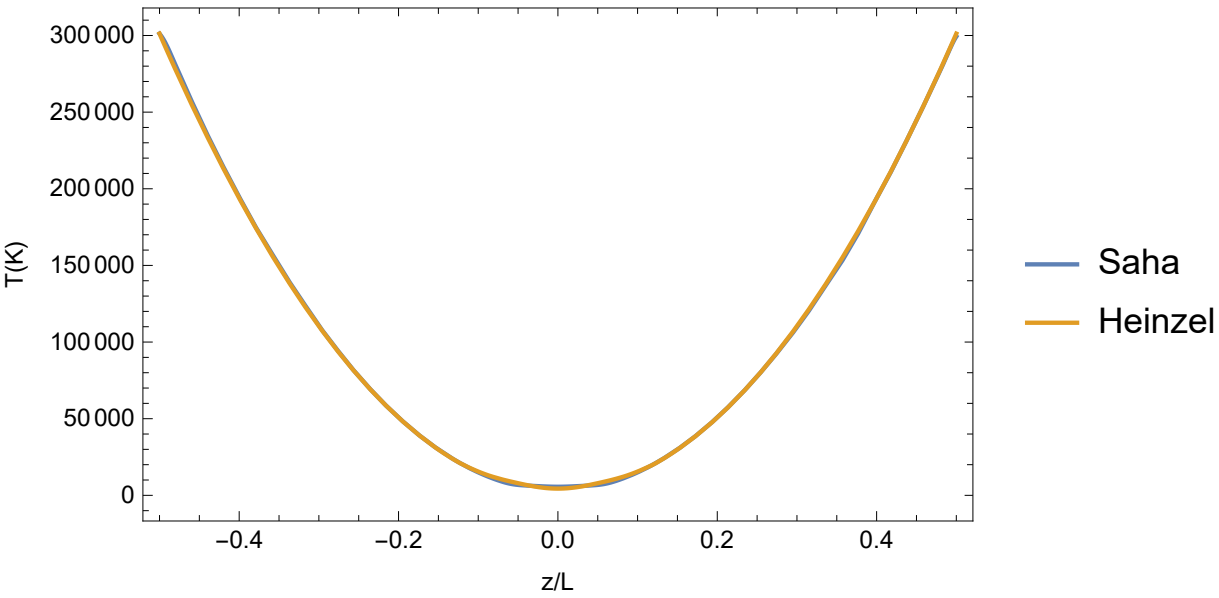

Figure 11: *Temperature profile along the thread for the Saha and Heinzel methods.*

2.3 Ohm's and ambipolar diffusions

Once we have calculated the profiles for the temperature and the ionisation, we calculate the Ohm η and ambipolar η_A diffusion for both methods which are defined as [35]

$$\eta = \frac{1}{\mu_0 \sigma}, \tag{2.5}$$

$$\eta_A = \frac{\xi_n^2}{\mu_0 \alpha_n} \tag{2.6}$$

where μ_0 is the vacuum magnetic permeability and $\xi_n = 1 - \xi_i$ is the neutral atoms fraction. The values of these dissipation coefficients are relevant for the efficiency of the wave damping.

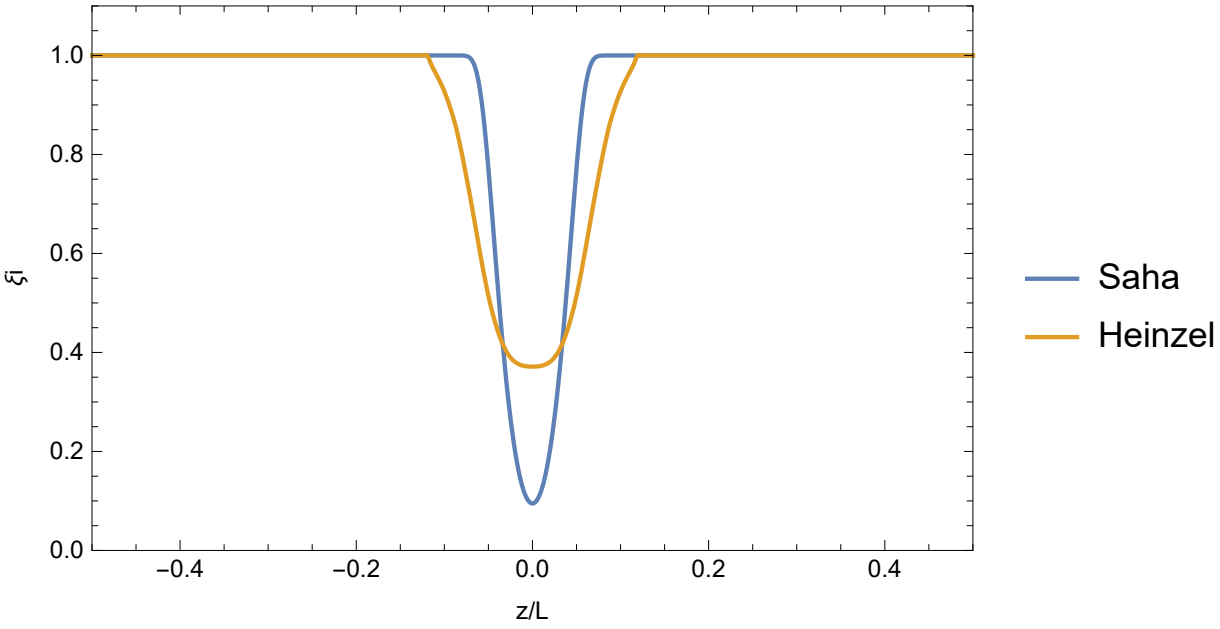

Figure 12: *Ionisation profile along the thread for the Saha and Heinzel methods.*

The Ohm coefficient is defined with the conductivity σ

$$\sigma = \frac{n_e e^2}{m_e(\nu'_{ei} + \nu'_{en})}, \tag{2.7}$$

where m_e and e are the electron mass and charge. ν'_{ei} and ν'_{en} are the effective electron-ion and electron-neutral collisional frequencies, respectively, and they are defined as

$$\nu'_{ei} = \frac{m_i}{m_i + m_e}\nu_{ei}, \quad \nu'_{en} = \frac{m_n}{m_n + m_e}\nu_{en}, \tag{2.8}$$

with ν_{ei} and ν_{en} being

$$\nu_{ei} = 3.7 \times 10^{-6}\frac{n_i \Lambda Z^2}{T^{3/2}}, \quad \nu_{en} = n_n\sqrt{\frac{8k_B T}{\pi m_{en}}}\Sigma_{en}, \tag{2.9}$$

where $\Lambda \approx 20$ is the Coulomb logarithm, Z is the atomic number, which is 1 for a hydrogen plasma, k_B is the Boltzmann constant and $\Sigma_{en} = 10^{-19}$ m^2 is the electron-neutral collision cross section, and n_i and n_n are the number density of the ions and neutrals respectively,

$$n_n = \frac{\rho_n}{m_n} = \frac{\xi_i \rho}{m_n} = \frac{(1-\xi_i)\rho}{m_p}, \quad n_i = \frac{\rho_i}{m_i} = \frac{\xi_i \rho}{m_p}, \tag{2.10}$$

and m_{en} is

$$m_{en} = \frac{m_e m_n}{m_e + m_n}, \tag{2.11}$$

The ambipolar coefficient depends on α_n that is the friction coefficient defined as

$$\alpha_n = \frac{1}{2}\xi_n(1-\xi_n)\frac{\rho_0^2}{m_n}\sqrt{\frac{16 k_B T}{\pi m_i}}\Sigma_{in}, \tag{2.12}$$

where $\Sigma_{in} = 5 \times 10^{-19}$ m^2 is the ion-neutral collision cross-section.

The profiles of the diffusion coefficients for both methods (Saha and Heinzel) are presented in Figure 13 for the Ohm diffusion coefficient and in Figure 14 for the ambipolar diffusion coefficient. For Ohm diffusion the Saha method has a lower maximum but the range where the coefficient has a significant value is slightly wider than in the Heinzel case. The ambipolar coefficient with the Saha method has the maximum at the centre of the thread, whereas with the Heinzel case the maximum is displaced and instead of a maximum there is a relative minimum at the centre of the thread. Comparing the results of the diffusions for both methods and assuming a magnetic field value of 10 G, the ambipolar diffusion is much larger than Ohm's diffusion, so the ambipolar term is expected to be dominant in the calculation of wave dissipation.

This simple estimation agrees with the previous results by, e.g., [6] regarding the efficiency of Ohm's and ambipolar diffusion in prominence conditions.

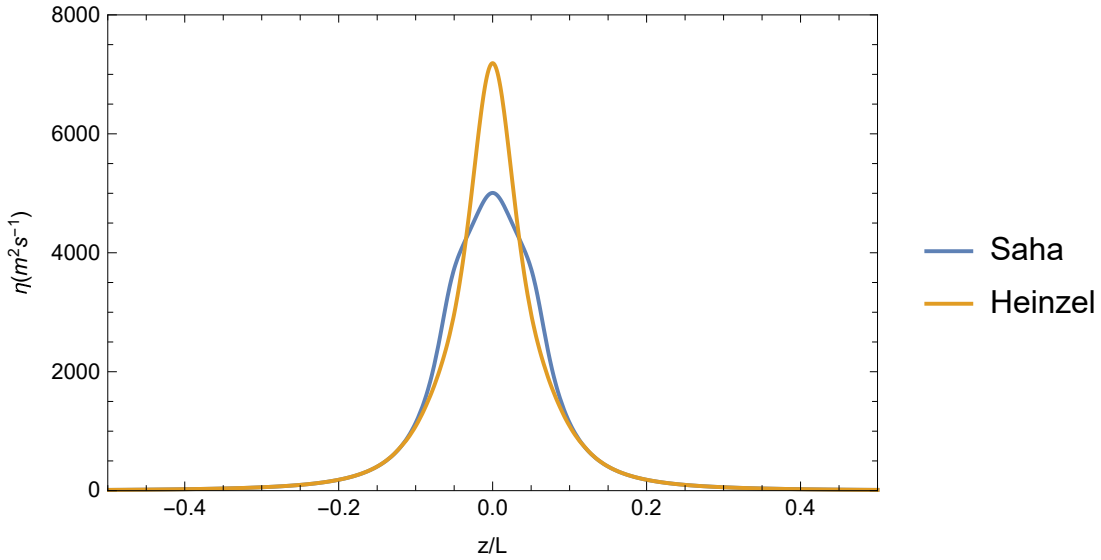

Figure 13: *Ohm diffusion coefficient for the Saha and Heinzel methods.*

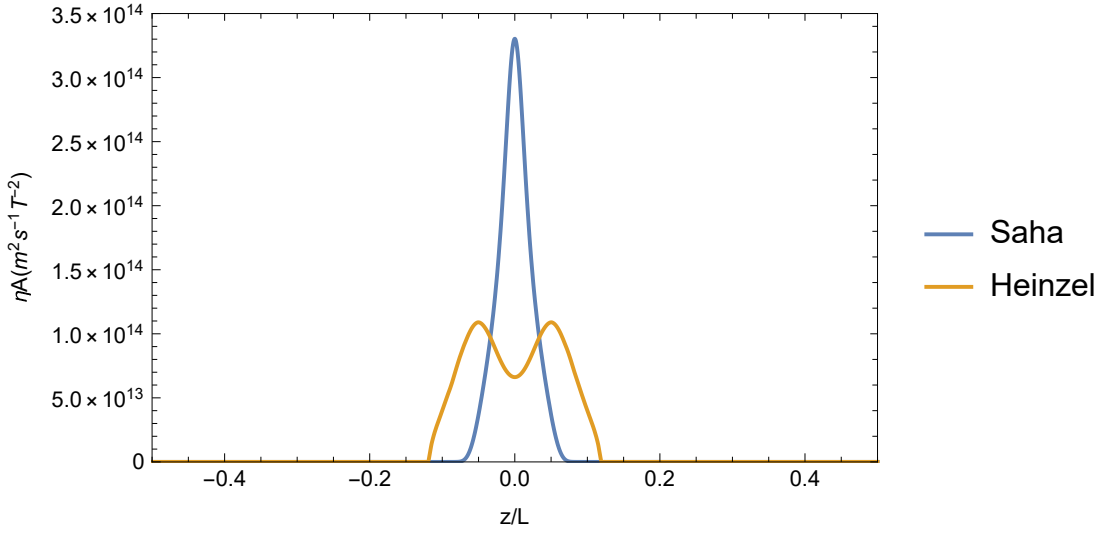

Figure 14: *Ambipolar diffusion coefficient for the Saha and Heinzel methods.*

3 MHD equations

Here we derive the basic equations that govern Alfvén waves in the 1D thread model.

Ionised plasmas are governed by magnetohydrodynamics (MHD), which combines the equations of the fluid mechanics with those of electromagnetism. For a single-fluid partially ionised plasma the MHD equations are the continuity Equation (3.1), the momentum Equation (3.2), the induction Equation (3.3) and the energy Equation (3.4) [4]. This set of equations is described as

$$\frac{D\rho}{Dt} = -\rho\vec{\nabla}\cdot\vec{v}, \tag{3.1}$$

$$\rho\frac{D\vec{v}}{Dt} = -\vec{\nabla}p + \frac{1}{\mu}\left(\vec{\nabla}\times\vec{B}\right)\times\vec{B} - \rho\vec{g} - \vec{\nabla}\cdot\Pi, \tag{3.2}$$

$$\begin{aligned}\frac{\partial\vec{B}}{\partial t} = \vec{\nabla}\times\left(\vec{v}\times\vec{B}\right) - \vec{\nabla}\times\left(\eta\vec{\nabla}\times\vec{B}\right) - \vec{\nabla}\times\left[\eta_H\left(\vec{\nabla}\times\vec{B}\right)\times\vec{B}\right] \\ +\vec{\nabla}\times\left\{\eta_A\left[\left(\vec{\nabla}\times\vec{B}\right)\times\vec{B}\right]\times\vec{B}\right\} - \vec{\nabla}\times\left[\tilde{\Xi}\vec{G}\times\vec{B}\right],\end{aligned} \tag{3.3}$$

$$\begin{aligned}\frac{Dp}{Dt} - \frac{\gamma p}{\rho}\frac{D\rho}{Dt} = (\gamma-1)\left[\vec{\nabla}\cdot\left(\kappa\vec{\nabla}T\right) - \rho L(T,\rho)\right] \\ +(\gamma-1)\left[\mu\eta|\vec{J}_{\parallel}|^2 + \mu(\eta+\eta_A)|\vec{J}_{\perp}|^2 + \sum_{m,n}\Pi_{mn}\frac{\partial v_m}{\partial x_n}\right],\end{aligned} \tag{3.4}$$

along with ideal gas Equation (2.4) and the condition $\vec{\nabla}\cdot\vec{B} = 0$.

In the equations $\vec{v}$ is the velocity and $\vec{B}$ is the magnetic field. $\frac{D}{Dt}$ is the total derivative and is defined as $\frac{D}{Dt} = \frac{\partial}{\partial t} + \vec{v}\cdot\vec{\nabla}$. In the momentum Equation $\vec{g}$ is the gravity and Π is the plasma viscosity tensor. In the induction Equation η_H is Hall's coefficient, $\vec{G}$ is the pressure function and $\tilde{\Xi}$ is the diamagnetic current coefficient. In the energy Equation the terms in the right are the thermal conduction, the radiative cooling, the Joule heating and the viscous heating. In this Equation κ is the thermal conductivity tensor, L is the heat-loss function, $\vec{J}_{\parallel}$ and $\vec{J}_{\perp}$ are the parallel and transverse components of the density current to the magnetic field direction and Π_{mn} are the components of the viscosity tensor.

We have presented the MHD equations in their most general form. However, in the present work we make some simplifications. We consider that there is no viscosity and the effect of external forces like the gravity is neglected. In the induction Equation we take into consideration the Ohm and ambipolar terms, neglecting the others. Concerning the energy Equation, it will not be used in our computations since Alfvén waves are incompressible, so that the energy Equation is replaced by the condition $\vec{\nabla}\cdot\vec{v} = 0$.

3.1 Linearisation and equations for Alfvén waves

Once we have take these considerations into account we linearise the equations in order to obtain an equation for the Alfvén waves. Alfvén waves are incompressible magnetic waves driven by magnetic tension force. They are polarised in the transverse direction to the magnetic field. They are a unique type of mode that appears in MHD. There is no counterpart of Alfvén waves in hydrodynamics. The linearisation of the MHD equations consists on assuming the form of the unknown magnitudes as

$$f(\vec{r},t) = f_0(\vec{r},t) + f_1(\vec{r},t),$$

where f_0 is the equilibrium term and f_1 is a perturbation. These magnitudes have the relation that $f_1 << f_0$. With these considerations we perturb $\vec{v}$, $\vec{B}$, p, ρ and T. The equilibrium values are the density profile for ρ_0, the constant pressure assumed in the model for p_0, the temperature profile for T_0, $\vec{v_0} = \vec{0}$ and $\vec{B}_0 = B_0\ \hat{z}$, with $B_0 = 10$ G.

We consider also that the velocity and the magnetic field perturbations, $\vec{v}_1$ and $\vec{B}_1$, are aligned in the y-direction, being transverse to the thread and all the unknowns are functions of t and z. With these final assumptions the perturbed unknowns are

$$p = p_0 + p_1(z,t), \tag{3.5}$$

$$\rho = \rho_0(z) + \rho_1(z,t), \tag{3.6}$$

$$T = T_0(z) + T_1(z,t), \tag{3.7}$$

$$\vec{v} = v_{1y}(z,t)\hat{y}, \tag{3.8}$$

$$\vec{B} = B_0\hat{z} + B_{1y}(z,t)\hat{y}. \tag{3.9}$$

Using the perturbed terms into Equations (3.1), (3.4) and (2.4), the results are

$$\frac{\partial \rho_1}{\partial t} = 0, \tag{3.10}$$

$$\frac{\partial p}{\partial t} = 0, \tag{3.11}$$

$$\frac{p_1}{p_0} = \frac{T_1}{T_0} + \frac{\rho_1}{\rho_0}. \tag{3.12}$$

Since we are studying the incompressible Alfvén waves, these three equations are decoupled from the momentum and induction equations.

The momentum Equation using the perturbed unknowns is written as

$$(\rho_0 + \rho_1)\frac{D\vec{v_1}}{Dt} = -\vec{\nabla}(p_0 + p_1) + \frac{1}{\mu}\left(\vec{\nabla} \times \left(\vec{B_0} + \vec{B_1}\right)\right) \times \left(\vec{B_0} + \vec{B_1}\right), \tag{3.13}$$

applying the linearisation the equation gets the form

$$\rho_0 \frac{\partial \vec{v_1}}{\partial t} = -\vec{\nabla} p_1 + \frac{1}{\mu}\left(\vec{\nabla} \times \vec{B_1}\right) \times \vec{B_0}. \tag{3.14}$$

Once we have linearised the equation we want to calculate the y-component of the equation decomposing the Lorentz force.

$$\vec{\nabla} \times \vec{B_1} = \begin{vmatrix} \hat{x} & \hat{y} & \hat{z} \\ \partial_x & \partial_y & \partial_z \\ 0 & B_{1y} & 0 \end{vmatrix} = -\frac{\partial B_{1y}}{\partial z}\hat{x}, \tag{3.15}$$

$$\left(\vec{\nabla} \times \vec{B_1}\right) \times \vec{B_0} = \begin{vmatrix} \hat{x} & \hat{y} & \hat{z} \\ -\frac{\partial B_{1y}}{\partial z} & 0 & 0 \\ 0 & 0 & B_0 \end{vmatrix} = B_0 \frac{\partial B_{1y}}{\partial z}\hat{y}, \tag{3.16}$$

the momentum Equation in the y-direction is written as

$$\rho_0 \frac{\partial v_{1y}}{\partial t} = \frac{B_0}{\mu}\frac{\partial B_{1y}}{\partial z}. \tag{3.17}$$

This is the first equation we need.

To obtain the second equation, we repeat the process for the induction Equation, which gets the form

$$\begin{aligned}\frac{\partial\left(\vec{B_0}+\vec{B_1}\right)}{\partial t} &= \vec{\nabla}\times\left(\vec{v_1}\times\left(\vec{B_0}+\vec{B_1}\right)\right)-\vec{\nabla}\times\left(\eta\vec{\nabla}\times\left(\vec{B_0}+\vec{B_1}\right)\right)\\ &+\vec{\nabla}\times\left\{\eta_A\left[\left(\vec{\nabla}\times\left(\vec{B_0}+\vec{B_1}\right)\right)\times\left(\vec{B_0}+\vec{B_1}\right)\right]\times\left(\vec{B_0}+\vec{B_1}\right)\right\},\end{aligned} \tag{3.18}$$

and with the linearisation rules the equation becomes

$$\frac{\partial\vec{B_1}}{\partial t}=\vec{\nabla}\times\left(\vec{v_1}\times\vec{B_0}\right)-\vec{\nabla}\times\left(\eta\vec{\nabla}\times\vec{B_1}\right)+\vec{\nabla}\times\left\{\eta_A\left[\left(\vec{\nabla}\times\vec{B_1}\right)\times\vec{B_0}\right]\times\vec{B_0}\right\}. \tag{3.19}$$

Once we have linearised the equation we want to obtain y-component as before. In order to obtain it, we calculate the advective, Ohm and ambipolar terms of the equation. The advective term is written as

$$\vec{v_1}\times\vec{B_0}=\begin{vmatrix}\hat{x}&\hat{y}&\hat{z}\\0&v_{1y}&0\\0&0&B_0\end{vmatrix}=B_0v_{1y}\hat{x}, \tag{3.20}$$

$$\vec{\nabla}\times\left(\vec{v_1}\times\vec{B_0}\right)=\begin{vmatrix}\hat{x}&\hat{y}&\hat{z}\\\partial_x&\partial_y&\partial_z\\B_0v_{1y}&0&0\end{vmatrix}=B_0\frac{\partial v_{1y}}{\partial z}\hat{y}. \tag{3.21}$$

Ohm's term is written down as

$$\vec{\nabla}\times\vec{B_1}=\begin{vmatrix}\hat{x}&\hat{y}&\hat{z}\\\partial_x&\partial_y&\partial_z\\0&B_{1y}&0\end{vmatrix}=-\frac{\partial B_{1y}}{\partial z}\hat{x}, \tag{3.22}$$

$$\vec{\nabla}\times\left(\eta\vec{\nabla}\times\vec{B_1}\right)=\begin{vmatrix}\hat{x}&\hat{y}&\hat{z}\\\partial_x&\partial_y&\partial_z\\-\eta\frac{\partial B_{1y}}{\partial z}&0&0\end{vmatrix}=-\frac{\partial}{\partial z}\left(\eta\frac{\partial B_{1y}}{\partial z}\right)\hat{y}=\left(-\frac{\partial\eta}{\partial z}\frac{\partial B_{1y}}{\partial z}-\eta\frac{\partial^2B_{1y}}{\partial z^2}\right)\hat{y}, \tag{3.23}$$

and the ambipolar term is described as

$$\left(\vec{\nabla}\times\vec{B_1}\right)\times\vec{B_0}=\begin{vmatrix}\hat{x}&\hat{y}&\hat{z}\\-\frac{\partial B_{1y}}{\partial z}&0&0\\0&0&B_0\end{vmatrix}=B_0\frac{\partial B_{1y}}{\partial z}\hat{y}, \tag{3.24}$$

$$\left[\left(\vec{\nabla}\times\vec{B_1}\right)\times\vec{B_0}\right]\times\vec{B_0}=\begin{vmatrix}\hat{x}&\hat{y}&\hat{z}\\0&B_0\frac{\partial B_{1y}}{\partial z}&0\\0&0&B_0\end{vmatrix}=B_0^2\frac{\partial B_{1y}}{\partial z}\hat{x}, \tag{3.25}$$

$$\begin{aligned}\vec{\nabla}\times\left\{\eta_A\left[\left(\vec{\nabla}\times\vec{B_1}\right)\times\vec{B_0}\right]\times\vec{B_0}\right\}&=\begin{vmatrix}\hat{x}&\hat{y}&\hat{z}\\\partial_x&\partial_y&\partial_z\\\eta_AB_0^2\frac{\partial B_{1y}}{\partial z}&0&0\end{vmatrix}=\\ \frac{\partial}{\partial z}\left(\eta_AB_0^2\frac{\partial B_{1y}}{\partial z}\right)\hat{y}&=\left(B_0^2\frac{\partial\eta_A}{\partial z}\frac{\partial B_{1y}}{\partial z}+B_0^2\eta_A\frac{\partial^2B_{1y}}{\partial z^2}\right)\hat{y},\end{aligned} \tag{3.26}$$

with all the terms decomposed, the linearised induction Equation in the y-direction is

$$\frac{\partial B_{1y}}{\partial t} = B_0 \frac{\partial v_{1y}}{\partial z} + \frac{\partial \eta}{\partial z}\frac{\partial B_{1y}}{\partial z} + \eta \frac{\partial^2 B_{1y}}{\partial z^2} + B_0^2 \frac{\partial \eta_A}{\partial z}\frac{\partial B_{1y}}{\partial z} + B_0^2 \eta_A \frac{\partial^2 B_{1y}}{\partial z^2}. \tag{3.27}$$

This is the second equation we were looking for.

3.2 Dimensionless equations

Once we have the linearised momentum and induction equations that govern Alfvén waves, we write them in dimensionless form. We define the Alfvén velocity, which is the velocity propagation of the Alfvén waves

$$V_A = \frac{B_0}{\sqrt{\mu\rho}}, \tag{3.28}$$

using the definition of V_A and the thread length L the dimensionless parameters are

$$\overline{z} = \frac{z}{L}, \quad \overline{t} = \frac{t}{L/V_{A0}}, \quad \overline{B_y} = \frac{B_{1y}}{B_0}, \quad \overline{v_y} = \frac{v_{1y}}{V_{A0}},$$

where V_{A0} is the Alfvén speed at the centre of the thread (z=0). The temporal and spatial derivatives are

$$\frac{\partial}{\partial t} = \frac{V_{A0}}{L}\frac{\partial}{\partial \overline{t}}, \quad \frac{\partial}{\partial z} = \frac{1}{L}\frac{\partial}{\partial \overline{z}},$$

With these parameters the dimensionless Equations (3.17) and (3.27) are

$$\frac{\partial \overline{v_y}}{\partial \overline{t}} = \left(\frac{V_A}{V_{A0}}\right)^2 \frac{\partial \overline{B_y}}{\partial \overline{z}}, \tag{3.29}$$

$$\frac{\partial \overline{B_y}}{\partial \overline{t}} = \frac{\partial \overline{v_y}}{\partial \overline{z}} + \frac{1}{V_{A0}L}\frac{\partial \eta}{\partial \overline{z}}\frac{\partial \overline{B_y}}{\partial \overline{z}} + \frac{\eta}{V_{A0}L}\frac{\partial^2 \overline{B_y}}{\partial \overline{z}^2} + \frac{B_0^2}{V_{A0}L}\frac{\partial \eta_A}{\partial \overline{z}}\frac{\partial \overline{B_y}}{\partial \overline{z}} + \frac{B_0^2 \eta_A}{V_{A0}L}\frac{\partial^2 \overline{B_y}}{\partial \overline{z}^2}. \tag{3.30}$$

We will study two cases of waves in the thread: first we will study standing modes. And then we will study propagating modes along the thread. Equations (3.29) and (3.30) are equally valid in both cases.

3.3 Standing modes

For the standing case we take the Fourier derivative for the temporal part

$$\frac{\partial}{\partial \overline{t}} \to -i\overline{\omega},$$

we redefine the magnetic field with

$$\overline{B'_y} \equiv i\overline{B_y},$$

with these adjustments Equations (3.29) and (3.30) get the form

$$\overline{\omega v_y} = \left(\frac{V_A}{V_{A0}}\right)^2 \frac{\partial \overline{B'_y}}{\partial \overline{z}}, \tag{3.31}$$

$$\overline{\omega}\overline{B'_y} = -\frac{\partial \overline{v_y}}{\partial \overline{z}} + i\left(\frac{1}{V_{A0}L}\frac{\partial \eta}{\partial \overline{z}}\frac{\partial \overline{B'_y}}{\partial \overline{z}} + \frac{\eta}{V_{A0}L}\frac{\partial^2 \overline{B'_y}}{\partial \overline{z}^2} + \frac{B_0^2}{V_{A0}L}\frac{\partial \eta_A}{\partial \overline{z}}\frac{\partial \overline{B'_y}}{\partial \overline{z}} + \frac{B_0^2 \eta_A}{V_{A0}L}\frac{\partial^2 \overline{B'_y}}{\partial \overline{z}^2}\right), \tag{3.32}$$

Equations (3.31) and (3.32) form an eigenvalue problem, where ω is the eigenvalue and $\overline{v_y}$ and $\overline{B_y'}$ are the eigenfunctions. For the standing modes, the eigenvalue will be numerically solved assuming as boundary conditions

$$\overline{v_y} = 0 \quad at \quad z = \pm L/2,$$
$$\frac{\partial \overline{B_y'}}{\partial \overline{z}} = 0 \quad at \quad z = \pm L/2.$$

3.4 Propagating modes

For the propagating case we take a temporal derivative in Equation (3.30) and we obtain

$$\frac{\partial^2 \overline{B_y}}{\partial \overline{t}^2} = \frac{\partial^2 \overline{v_y}}{\partial \overline{z} \partial \overline{t}} + \frac{1}{V_{A0} L} \frac{\partial \eta}{\partial \overline{z}} \frac{\partial^2 \overline{B_y}}{\partial \overline{z} \partial \overline{t}} + \frac{\eta}{V_{A0} L} \frac{\partial^3 \overline{B_y}}{\partial \overline{z}^2 \partial \overline{t}} + \frac{B_0^2}{V_{A0} L} \frac{\partial \eta_A}{\partial \overline{z}} \frac{\partial^2 \overline{B_y}}{\partial \overline{z} \partial \overline{t}} + \frac{B_0^2 \eta_A}{V_{A0} L} \frac{\partial^3 \overline{B_y}}{\partial \overline{z}^2 \partial \overline{t}}, \tag{3.33}$$

in order to have the equation in terms of the magnetic field perturbation alone we use Equation (3.29) and the result is

$$\begin{aligned} \frac{\partial^2 \overline{B_y}}{\partial \overline{t}^2} = \frac{\partial}{\partial \overline{z}} \left[\left(\frac{V_A}{V_{A0}} \right)^2 \frac{\partial \overline{B_y}}{\partial \overline{z}} \right] + \frac{1}{V_{A0} L} \frac{\partial \eta}{\partial \overline{z}} \frac{\partial^2 \overline{B_y}}{\partial \overline{z} \partial \overline{t}} \\ + \frac{\eta}{V_{A0} L} \frac{\partial^3 \overline{B_y}}{\partial \overline{z}^2 \partial \overline{t}} + \frac{B_0^2}{V_{A0} L} \frac{\partial \eta_A}{\partial \overline{z}} \frac{\partial^2 \overline{B_y}}{\partial \overline{z} \partial \overline{t}} + \frac{B_0^2 \eta_A}{V_{A0} L} \frac{\partial^3 \overline{B_y}}{\partial \overline{z}^2 \partial \overline{t}}, \end{aligned} \tag{3.34}$$

we use the temporal Fourier derivative and we obtain

$$\left(\overline{V_A}^2 - \frac{i \overline{\omega} \eta}{V_{A0} L} - \frac{i \overline{\omega} B_0^2 \eta_A}{V_{A0} L} \right) \frac{\partial^2 \overline{B_y}}{\partial \overline{z}^2} + \left(2 \overline{V_A} \frac{\partial \overline{V_A}}{\partial \overline{z}} - \frac{i \overline{\omega}}{V_{A0} L} \frac{\partial \eta}{\partial \overline{z}} - \frac{i \overline{\omega} B_0^2}{V_{A0} L} \frac{\partial \eta_A}{\partial \overline{z}} \right) \frac{\partial \overline{B_y}}{\partial \overline{z}} + \overline{\omega}^2 \overline{B_y} = 0. \tag{3.35}$$

To solve this equation, we shall assume that the waves are driven at $z = -L/2$ with an arbitrary amplitude and a prescribed frequency, ω. The boundary condition at $z = L/2$ will be imposed according to the behaviour of the energy flux. This is explained later.

3.5 Numerical method

For this work we have solved the equations using the numerical symbolic program Mathematica. We used several notebooks where we calculated the solutions we need.

In order to obtain the temperature and ionisation profiles, for the Saha method we have used the module FindRoot using Equations (2.2) and (2.4) with 1000 points in the thread. For the Heinzel method we have interpolated first the numerical values of Table 2 and then we have used again FindRoot with the interpolated function and Equation (2.4). Once we have obtained the profiles we have interpolated and smoothed them. Using the interpolated functions, we have obtained the Ohm and ambipolar diffusion coefficients.

For the standing modes case, we have used the module NDEigensystem, where we have obtained a list of frequencies and their corresponding eigenfunctions of the velocity and magnetic field perturbations.

For the propagating mode case, we have implemented the module of NDSolve, where we have solved the Equation (3.35) using different boundary conditions. This equations has been solved for 1000 different frequencies.

4 Results

4.1 Standing modes

First, we start to study the case of standing waves. In this case, the frequency of the different modes has to be determined by integrating the governing equations along the thread and imposing appropriate boundary conditions at the thread ends. As stated before, for standing Alfvén waves, these boundary conditions are that the velocity perturbation and the spatial derivative of the magnetic field perturbation are both zero. Dimensionless units are used throughout this section.

The numerical method to compute the eigenvalues, based on a Mathematica routine, produces some spurious results. To identify and remove them, we have checked their eigenfunctions and have seen that they are basically noise. So we have deleted these unphysical solutions and have considered the physically meaningful results only.

We use Equations (3.29) and (3.30) to obtain the standing modes solutions for the Saha and Heinzel methods. Since this system along with the above-stated boundary conditions is an eigenvalue problem, we have obtained the eigenvalues, which are the frequencies of the modes, and the eigenfunctions, which are the velocity and the magnetic field perturbations.

4.1.1 Eigenvalues

The eigenvalues obtained can have positive and negative values. We drop out the negative values because they represent the same results as the positive ones. The eigenvalues have real and imaginary parts. The real and imaginary parts of the first 16 eigenvalues are plotted in Figure 15 for both Saha and Heinzel methods.

The real part of the eigenfrequencies increases linearly with the mode number for both methods, whereas the imaginary part has dependence similar to a parabola. In the imaginary part the result of the Saha method is slightly nonmonotic with the mode number, and the Heinzel method gives a monotonically increasing behaviour. The values of the imaginary part are much lower than those of the real part for both methods which indicates a weak damping, and the Saha method damping rates are higher than the Heinzel method ones.

4.1.2 Eigenfunctions

For the eigenfunctions, we took the first 5 eigenfunctions for both methods and plotted their absolute value in Figures 16 and 17.

In these set of plots we see that the results are almost identical for both methods. The results are normalised in order to have a maximum value of 1 for the absolute value of the velocity.

The velocity functions have a form similar to a harmonic function with a spatially-dependent amplitude. The harmonic number corresponding to each function is revealed by counting the numbers of peaks the functions have, corresponding to the mode number plus 1, being for example the fundamental mode with one peak and the third harmonic with four peaks. We see that the higher the harmonic, the further the maximum value of the function is located away from the centre and the smaller the internal peaks are.

The magnetic field pertubation behaves in a similar way as the velocity, since each function has a number of peaks corresponding to their mode number, but in this case we do not need to add 1. The fundamental mode has no peak, whereas for instance the second harmonic has two peaks. We also see that the amplitude of the magnetic field perturbation at the ends of the thread is bigger when the harmonic number is lower. The behaviour of the magnetic field perturbation is related with the derivative of the velocity, as seen in Equation (3.29).

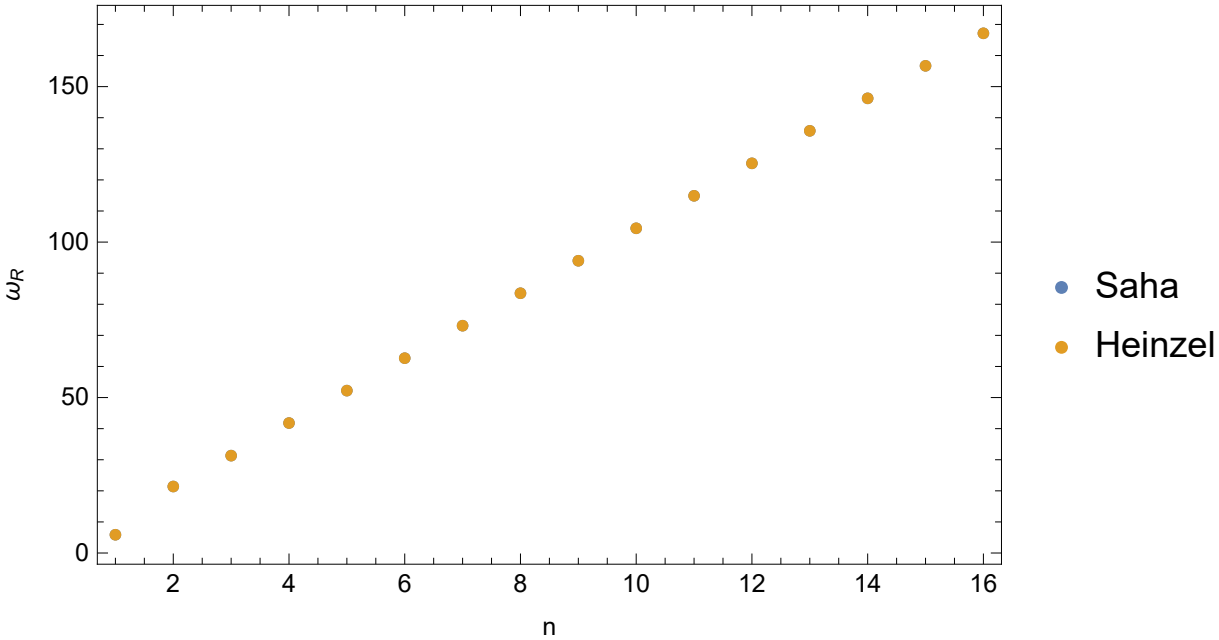

(a) Real part

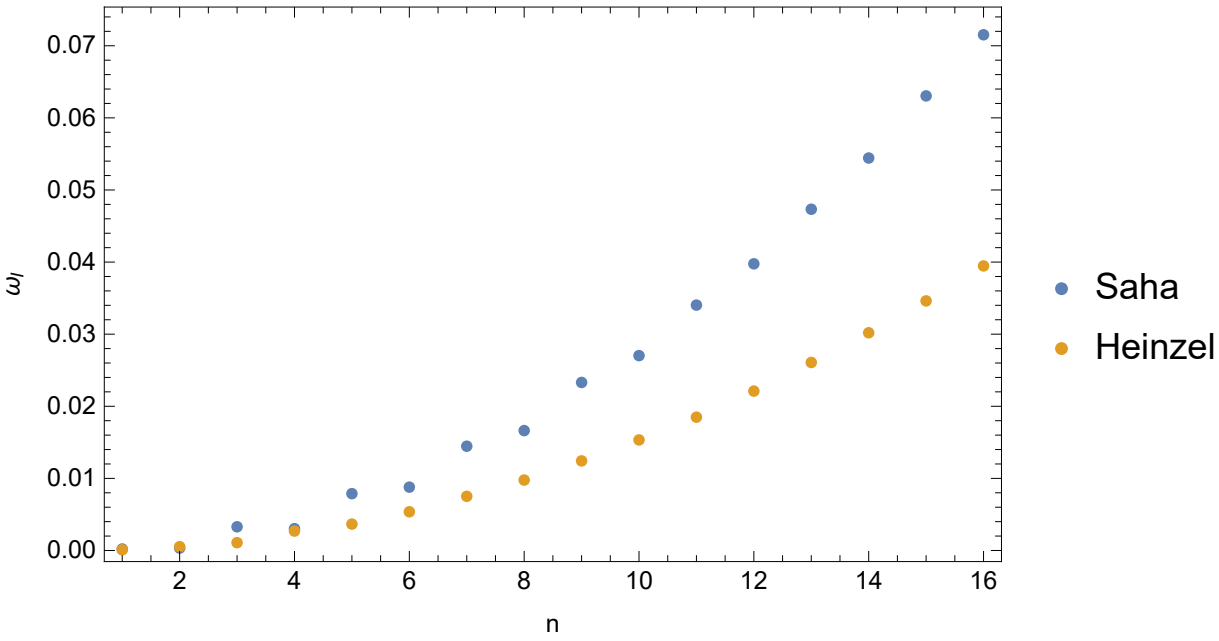

(b) Imaginary part

Figure 15: *Real and imaginary part of the eigenvalues for Saha and Heinzel methods. Dimensionless units are used.*

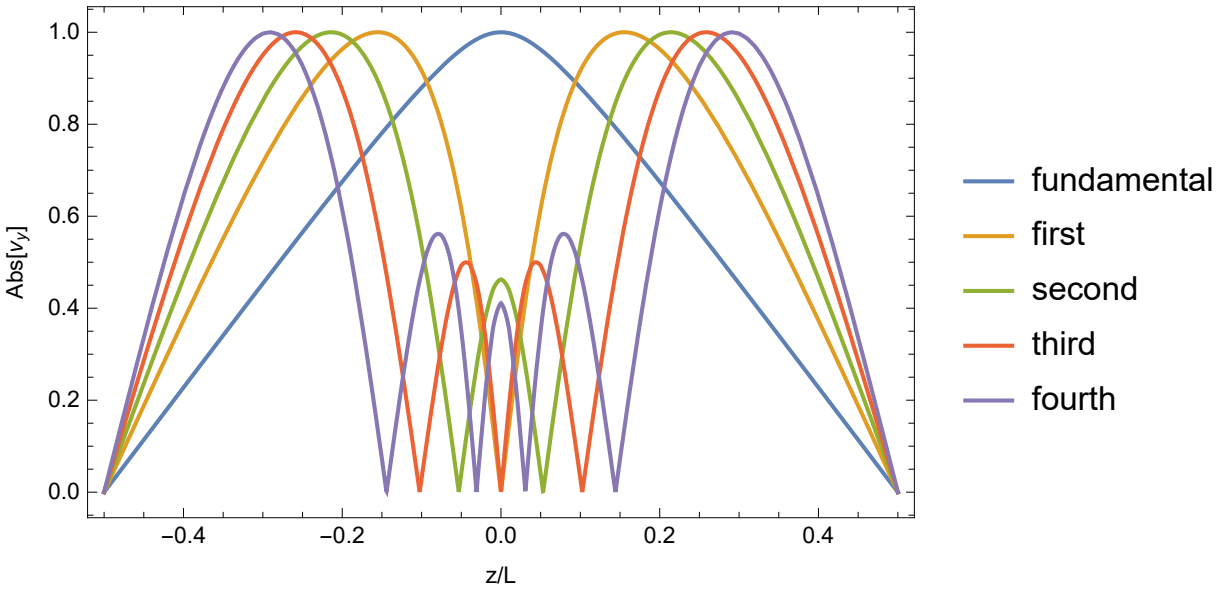

(a) Saha

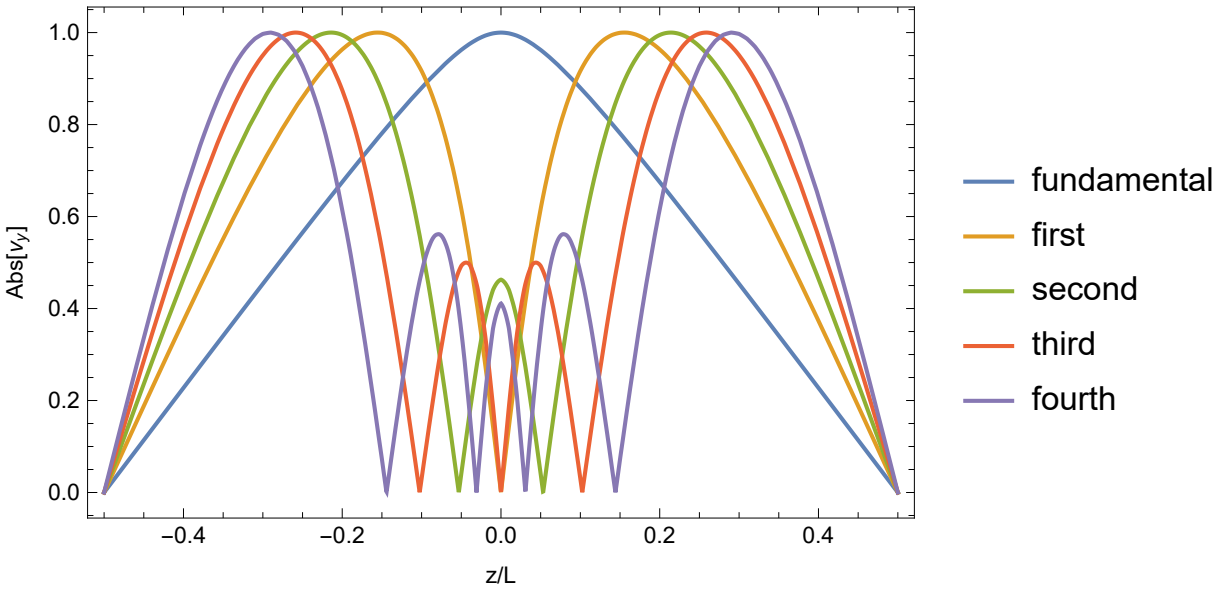

(b) Heinzel

Figure 16: *Absolute value of the velocity perturbation for Saha and Heinzel methods. Arbitrary units are used so that* $|v_y| = 1$.

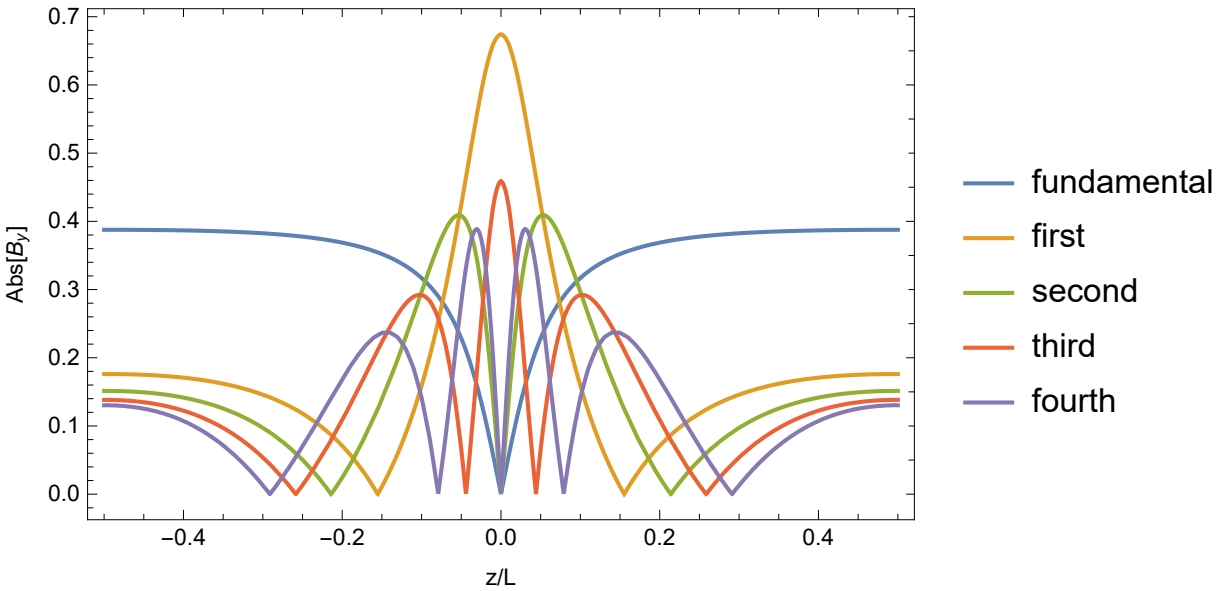

(a) Saha

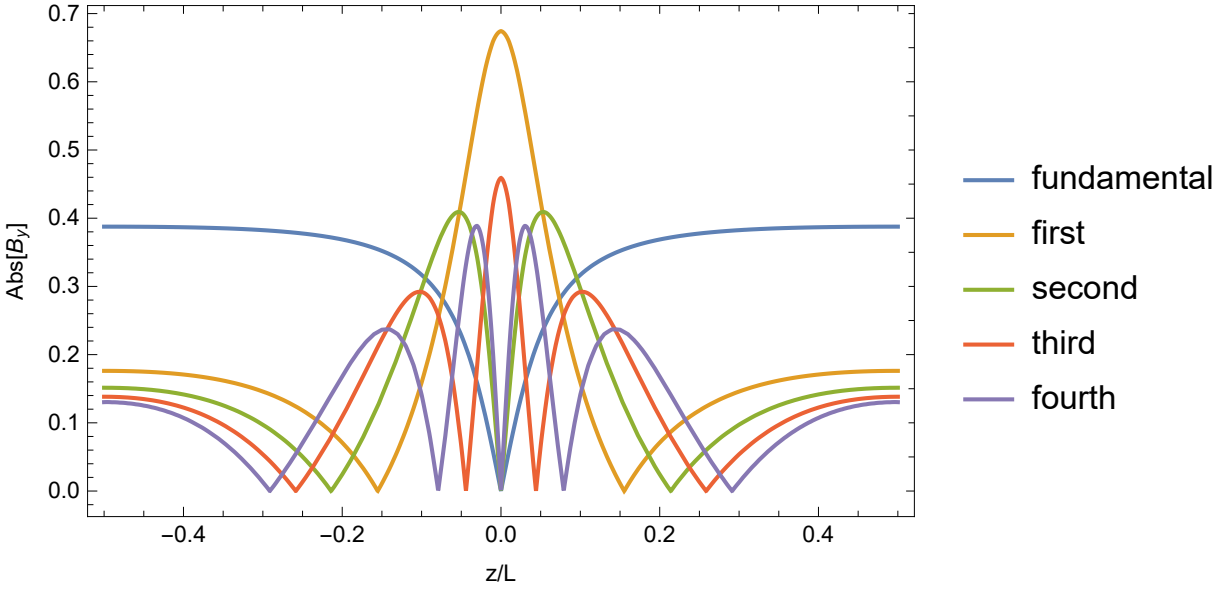

(b) Heinzel

Figure 17: *Absolute value of the magnetic field perturbation for Saha and Heinzel methods. The same normalisation of 16 is used.*

The standing modes could be classified into different types according to the location of the maximum value of the velocity perturbation. These two types are the internal modes if the maximum is in the partially ionised dense region or the external modes if the maximum is in the totally ionised evacuated region [29], [18].

After looking at the functions of Figure 16 we see that the fundamental mode is the only one that may be classified as an internal (or even hybrid) mode, because it is the only mode that has its maximum in the partially ionised region of the thread, whereas the other modes are external because their maxima are in the totally ionised region. This conclusion is the same for both methods. We point out that the classification of [29] was done for a model with a piecewise constant density, whereas in the present model the density changes continuously along the thread. So, the mode classification of [29] may not be entirely applicable here.

4.1.3 Period, damping time and damping per period

Once we have looked at the eigenfrequencies and the eigenfunctions, we can calculate the period, damping time and damping per period. These three quantities are defined as

$$P = \frac{2\pi}{\omega_R}, \quad \tau_D = \frac{1}{|\omega_I|}, \quad D_P = \frac{\tau_D}{P},$$

where ω_R and ω_I are the real and imaginary parts of the eigenfrequencies respectively. We plot them in terms of the mode number and normalise P and τ_D with respect to the period and damping time of the fundamental mode respectively. In physical units, the values of P and τ_D of the fundamental mode are 20 minutes, and 1.26×10^5 minutes, respectively. The plots are in Figure 18a for the period, Figure 18b for the damping time and Figure 19 for the damping per period.

The normalised period decreases with the mode number for both methods, which agrees with the fact that the real part of the fundamental mode frequency is the smallest one and the period is the inverse of the real part of the eigenfrequencies. This results are the same for both methods since the real part of the frequency has almost the same value for both methods and the small differences are not noticeable in this plot.

The damping time also decreases with the mode number, but in the Saha method it evolves in a nonmonotic way. This is due to the behaviour of the imaginary part of the frequencies.

The damping per period defines the efficiency of the damping. In Figure 19 we see that for both methods the damping is more efficient for high values of the mode number. However, the behaviour depends on which method we are considering. For the Saha method the evolution of D_p is nonmonotic, being its maximum in the first harmonic. For the Heinzel method the evolution is in a monotic way, being the maximum located in the fundamental mode. With exception of the first harmonic, the Heinzel method gives higher values of the damping per period, which corresponds to smaller efficiency of the damping. We notice that the damping times obtained here are significantly larger than those reported in the observations. Only harmonics of very large order are efficiently damped.

4.1.4 Energy balance

Once we have looked at the eigenfrequencies and the eigenfunctions, we do an energy analysis. This analysis is done by comparing the Joule heating associated with the dissipation of the standing Alfvén waves and the cooling produced by the thermal radiation of the plasma.

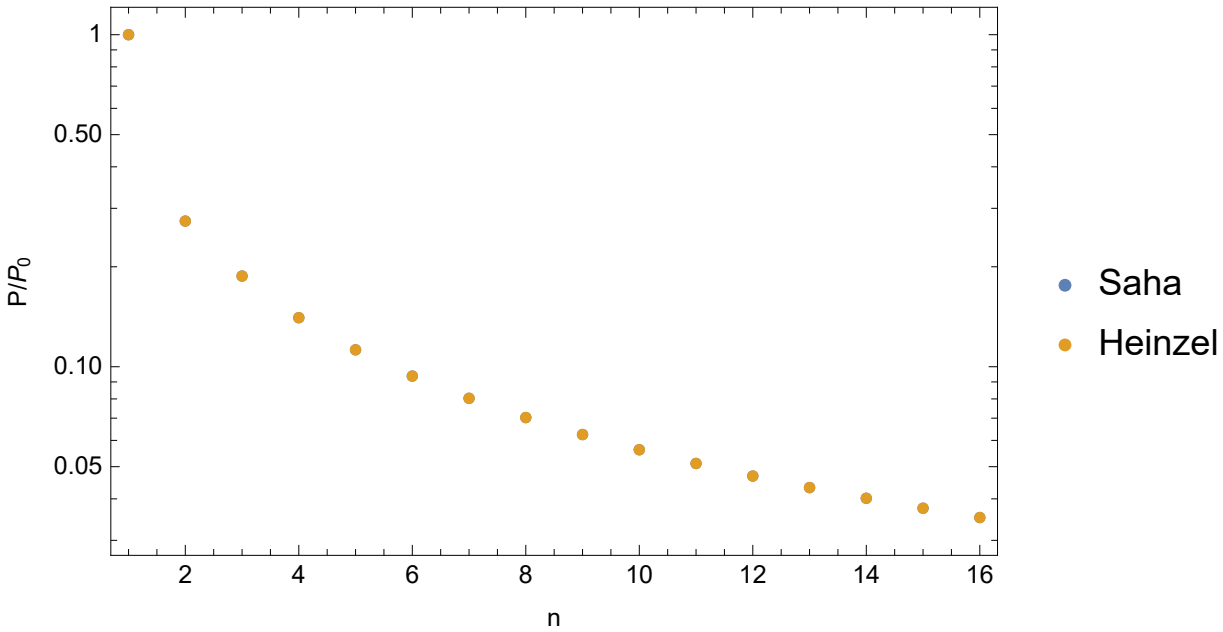

(a) Real part

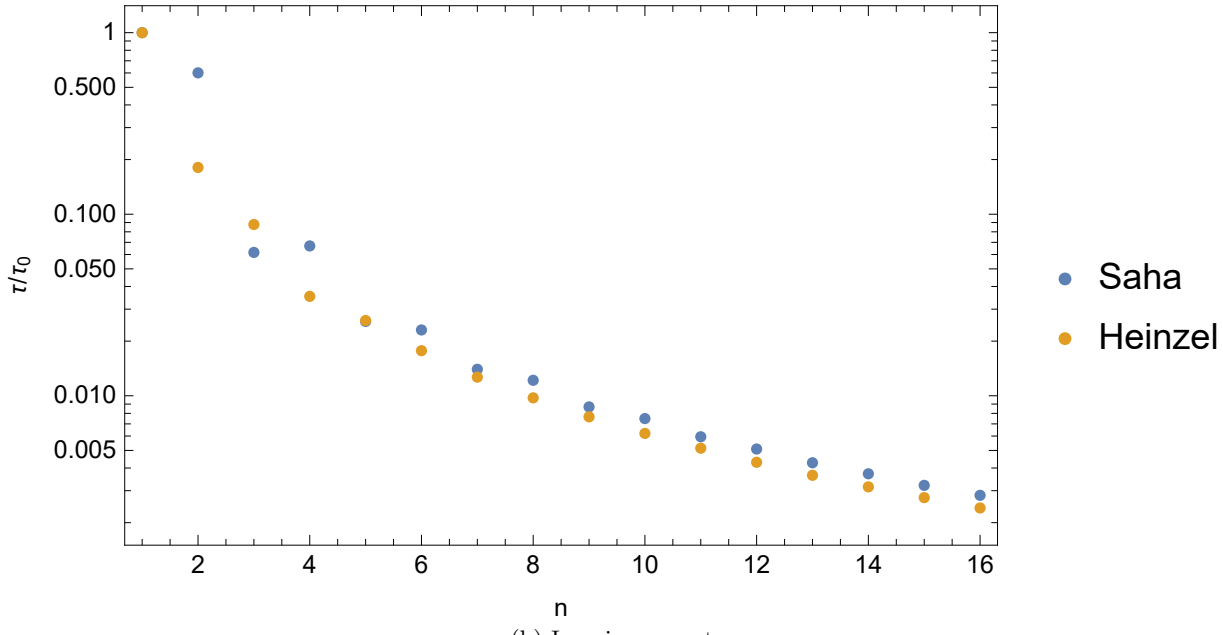

(b) Imaginary part

Figure 18: *Normalised period and damping time as functions of the mode number.* P_0 *and* τ_0 *are the corresponding quantities of the fundamental mode.*

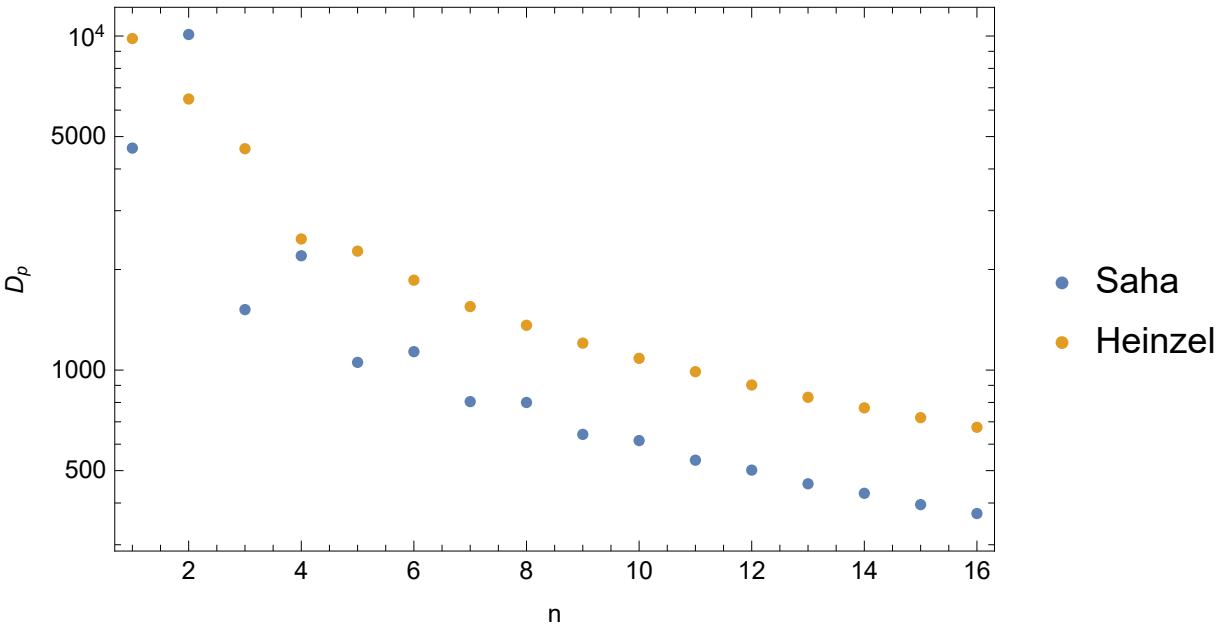

Figure 19: *Damping per period as a function of the mode number.*

The Joule heating term takes into account plasma heating due to the dissipation of electric currents. The Joule heating can be decomposed as

$$\vec{J} \cdot \vec{E}^* = \mu_0 \eta |\vec{J}_{\parallel}|^2 + \mu_0(\eta + B_0^2 \eta_A)|\vec{J}_{\perp}|^2, \tag{4.1}$$

where $J_{\parallel}$ and $J_{\perp}$ are the parallel and perpendicular components of the electric current. They are defined as

$$\vec{J}_{\parallel} = \frac{1}{\mu_0}\left[\left(\vec{\nabla} \times \vec{B}\right) \cdot \frac{\vec{B}}{|\vec{B}|}\right], \tag{4.2}$$

$$\vec{J}_{\perp} = \frac{1}{\mu_0}\frac{\vec{B}}{|\vec{B}|} \times \left[\left(\vec{\nabla} \times \vec{B}\right) \times \frac{\vec{B}}{|\vec{B}|}\right]. \tag{4.3}$$

In our case the magnetic field perturbation has only one component, which is the y-direction. Using Equations (4.2) and (4.3) we can calculate the dot and cross product of the magnetic field curl and its unitary vector.

$$\left(\vec{\nabla} \times \vec{B}\right) \cdot \frac{\vec{B}}{|\vec{B}|} = 0, \tag{4.4}$$

$$\left(\vec{\nabla} \times \vec{B}\right) \times \frac{\vec{B}}{|\vec{B}|} = \begin{vmatrix} \hat{x} & \hat{y} & \hat{z} \\ -\partial_z B_y & 0 & 0 \\ 0 & 1 & 0 \end{vmatrix} = -\frac{\partial B_y}{\partial z}\hat{z}. \tag{4.5}$$

We see that the parallel component does not contribute to the heating, since the magnetic field and the electric current are orthogonal. The perpendicular component of the electric component has the value of

$$J_{\perp} = \frac{1}{\mu_0}\begin{vmatrix} \hat{x} & \hat{y} & \hat{z} \\ 0 & 1 & 0 \\ 0 & 0 & -\partial_z B_y \end{vmatrix} = -\frac{1}{\mu_0}\frac{\partial B_y}{\partial z}\hat{x}. \tag{4.6}$$

Once we have calculated the components of the electric current, we can write down the Joule heating, which has the form of

$$\vec{J}\cdot\vec{E}^{*}=\frac{\eta+B_0^2\eta_A}{\mu_0}\left|\frac{\partial B_y}{\partial z}\right|^2. \tag{4.7}$$

We want to have the heating function in terms of the dimensionless magnetic field, so we use the definitions of the dimensionless magnetic field and z. We put also a factor 2 dividing because the heating rate must be averaged in a complete period of the wave to obtain the hot rate. The temporal average of a complex exponential type dependence introduces a factor 1/2.

With these assumptions, the heating function is written down as

$$\vec{J}\cdot\vec{E}^{*}=\left(\frac{B_0}{L}\right)^2\frac{\eta+B_0^2\eta_A}{2\mu_0}\left|\frac{\partial\overline{B'_y}}{\partial\overline{z}}\right|^2. \tag{4.8}$$

In order to have a realistic value of the velocity, we multiply the heating function with a typical value of the velocity amplitude of 1 $\mathrm{km\,s^{-1}}$, and this value is divided V_{A0} in order to keep the units of the heating function consistently. With these assumptions we finally write the heating function, which takes the form of

$$\vec{J}\cdot\vec{E}^{*}=\left(\frac{10^3}{V_{A0}}\right)^2\left(\frac{B_0}{L}\right)^2\frac{\eta+B_0^2\eta_A}{2\mu_0}\left|\frac{\partial\overline{B'_y}}{\partial\overline{z}}\right|^2. \tag{4.9}$$

For the cooling by radiation, we will use two different approaches. The first one is based on the optically-thin approximation using the semi-empirical parametrisation of Hildner, and the second one is based on the Athay function, which may provide a more realistic representation of the cooling in the densest part of the thread.

Hildner [15] considers the following form of the cooling function

$$\rho L(\rho,T)=\rho^2\chi^{*}T^{\alpha}, \tag{4.10}$$

where χ^* and α are piecewise parameters that depend on the temperature. The parametrisation of the Hildner cooling function is given in Table 3.

Temperature range (K)	χ^*	α
$T\leq 15\times10^3$	1.76×10^{-13}	7.4
$15\times10^3<T\leq 8\times10^4$	4.29×10^{10}	1.8
$8\times10^4<T\leq 3\times10^5$	2.86×10^{19}	0.0
$3\times10^5<T\leq 8\times10^5$	1.41×10^{33}	-2.5
$T>8\times10^5$	1.97×10^{24}	-1.0

Table 3: Values in MKS units of the piecewise parameters in terms of the temperature for the Hildner cooling function.

In Athay [3], the cooling function is given by

$$\rho L(\rho,T)=f_p^{Athay}(T)\frac{\rho^2T^2}{m_p^2}, \tag{4.11}$$

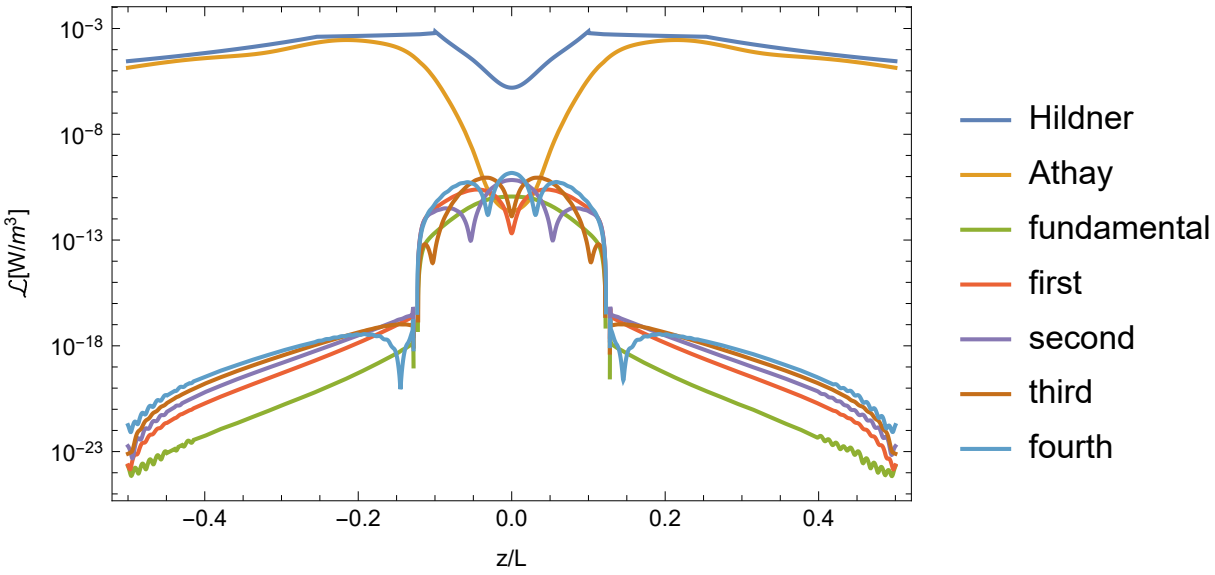

(a) Saha

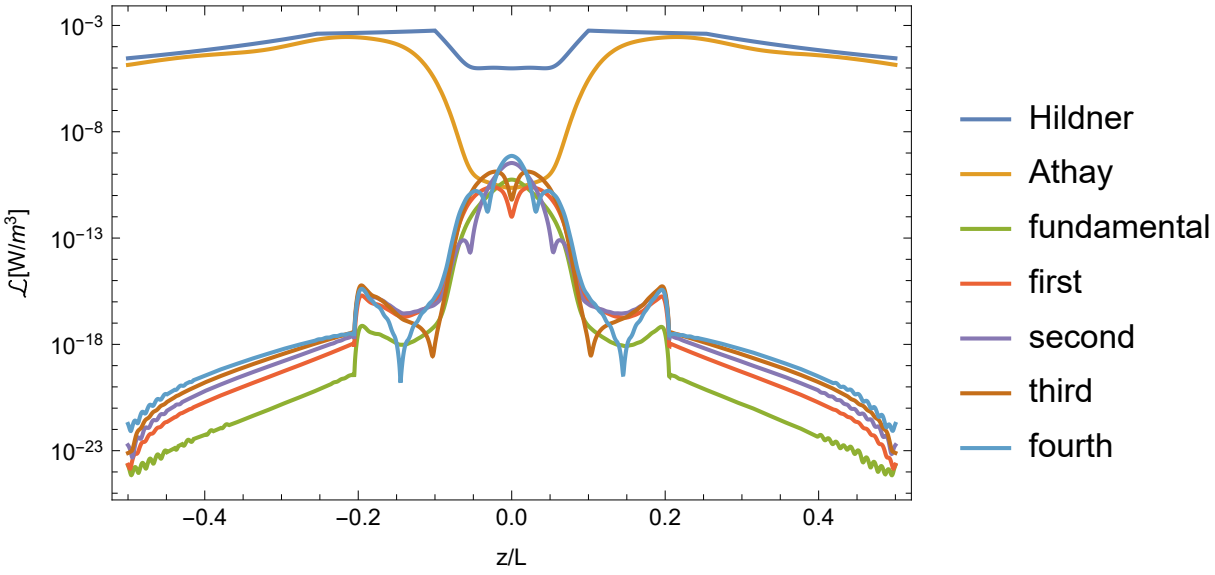

(b) Heinzel

Figure 20: *Heating profiles in Saha and Heinzel methods compared with radiation losses.*

where m_p is the proton mass and f_p^{Athay} is an analytic function of the temperature which is written, in MKS units, as

$$f_p^{Athay} = 10^{-35} T^{-2} \Big\{ 0.4 \exp\left[-30\left(\log_{10} T - 4.6\right)^2\right] + 4 \exp\left[-20\left(\log_{10} T - 4.9\right)^2\right] + 4.5 \exp\left[-16\left(\log_{10} T - 5.35\right)^2\right] + 2 \exp\left[-4\left(\log_{10} T - 6.1\right)^2\right] \Big\} \tag{4.12}$$

Once we have defined the heating and cooling functions, we calculate the functions for both methods, namely Saha and Heinzel. The results are displayed in Figure 20. In these figures we plot the heating functions of the first five eigenmodes together with the Hildner and Athay cooling functions. The plots are in logarithmic scale.

The heating functions due to the Joule effect have a similar behaviour for both methods, being their highest value at the centre of the thread and their minimums at their ends. The region

with higher heating values is located in the range of $z/L \in (-0.15, 0.15)$ approximately. This is consistent with the spatial dependence of the Ohm and ambipolar coefficients as explained in Section 2.3. The maximum value of the heating functions depends on what particular harmonic we are considering, so that the higher the harmonic, the larger the maximum heating.

For the cooling function, both functions give similar results in the hot part of the thread, but the Hildner functions gives higher values than the Athay functions specially in the coolest and densest part of the thread, i.e., the centre. Cooling is higher in the evacuated part of the thread and attains minimum values at the centre. The main difference between the Saha and Heinzel method is that the functions in the Saha methods had faster decrease at the centre.

Comparing the cooling and the heating functions, we see that the cooling functions have much higher values than the heating functions, specially in the hot coronal part of the thread. In conclusion, the heating produced by the Joule effect does not compensate the cooling produced by radiation in the hot part of the thread. However, in the cool centre of the thread, the Joule dissipation attains its maximum and may compensate the radiative losses if those are represented by the Athay function, which in principle is more realistic than the Hildner function in cool plasmas. Therefore, dissipation of standing Alfvén waves could have a local impact on the energy balance in the densest and coolest part of the thread, while it would be negligible in the hotter part. Finally, we recall that we have assumed a velocity amplitude of 1 $\mathrm{km\,s^{-1}}$ for all modes. If a larger/smaller amplitude is considered, the associated heating would consequently be larger/smaller. The dependence is quadratic in the velocity amplitude.

4.2 Propagating modes

Now we turn to the case of propagating waves. We use Equation (3.34) in order to solve the spatial dependence of the magnetic field perturbation in the thread for a given wave frequency. This Equation is solved for both Saha and Heinzel methods. We have solved the equation for 1000 different frequencies, ranging from 0.2 to 200 in dimensionless units. We assume that waves are driven at the left end of the thread, i.e., at $z = -L/2$, with an arbitrary amplitude, while at the right end of the thread ($z = L/2$) we assume a boundary condition based on the behaviour of the energy flux.

The energy flux of an Alfvén wave averaged over one full period of the wave is given by

$$\langle \vec{\pi} \rangle = -\frac{1}{2\mu_0} \mathrm{Re}\left[v_{1y} B_{1y}^{*} \right] \vec{B}_0, \tag{4.13}$$

where * denotes the complex conjugate.

The energy flux can be separated into the parallel and anti-parallel contributions with respect to the magnetic field direction, which are written down as $\langle \vec{\pi} \rangle^{\uparrow}$ and $\langle \vec{\pi} \rangle^{\downarrow}$ respectively. In order to write these contributions, we use the Elsässer variables, which are defined as

$$z^{\uparrow} = v_{1y} - \frac{B_{1y}}{\sqrt{\mu_0 \rho}}, \tag{4.14}$$

that represents a parallel-propagating disturbance, and

$$z^{\downarrow} = v_{1y} + \frac{B_{1y}}{\sqrt{\mu_0 \rho}}, \tag{4.15}$$

that represents an anti-parallel-propagating disturbance.

With these new variables we can write the energy flux as $\langle\vec{\pi}\rangle = \langle\vec{\pi}\rangle^{\uparrow} - \langle\vec{\pi}\rangle^{\downarrow}$, where

$$\langle\vec{\pi}\rangle^{\uparrow} = \frac{1}{8}\sqrt{\frac{\rho}{\mu_0}}z^{\uparrow}(z^{\uparrow})^{*}\vec{B}_0, \tag{4.16}$$

$$\langle\vec{\pi}\rangle^{\downarrow} = \frac{1}{8}\sqrt{\frac{\rho}{\mu_0}}z^{\downarrow}(z^{\downarrow})^{*}\vec{B}_0. \tag{4.17}$$

The boundary condition at $z = L/2$ can be set according to the behaviour of the energy flux. The examples are the perfectly reflecting boundary and the perfectly transparent boundary. In the perfectly reflecting boundary $\langle\vec{\pi}\rangle^{\uparrow} = \langle\vec{\pi}\rangle^{\downarrow}$, Then

$$\langle\vec{\pi}\rangle = \langle\vec{\pi}\rangle^{\uparrow} - \langle\vec{\pi}\rangle^{\downarrow} = 0. \tag{4.18}$$

This condition requires that $v_{1y}B_{1y}^{*} = 0$. If B_{1y} is arbitrary, then $v_{1y} = 0$. Using Equation (3.29) we obtain

$$v_{1y} = \frac{i}{\omega}\frac{B_0}{\mu\rho}\frac{\partial B_{1y}}{\partial z} = 0 \Rightarrow \frac{\partial B_{1y}}{\partial z} = 0, \tag{4.19}$$

In the perfectly transparent boundary, we have

$$\langle\vec{\pi}\rangle^{\uparrow} \neq 0, \quad \langle\vec{\pi}\rangle^{\downarrow} = 0,$$

which is equivalent to $z^{\downarrow} = 0$. Using Equation (4.15) we obtain

$$z^{\downarrow} = v_{1y} + \frac{B_{1y}}{\sqrt{\mu_0\rho}} = 0,$$

$$\frac{i}{\omega}\frac{B_0}{\mu_0\rho}\frac{\partial B_{1y}}{\partial z} + \frac{B_{1y}}{\sqrt{\mu_0\rho}} = 0 \Rightarrow \frac{\partial B_{1y}}{\partial z} = \frac{i\omega}{v_A}B_{1y}.$$

In general, a realistic boundary condition would be neither perfectly reflecting nor perfectly transparent. So we can define a general boundary condition as

$$\frac{\partial B_y}{\partial z} = \varepsilon\frac{i\omega}{v_A}B_{1y}, \tag{4.20}$$

where $\varepsilon \in [0, 1]$ is a parameter. Checking the extreme cases for ε we obtain

$$\varepsilon = 0 \rightarrow \frac{\partial B_y}{\partial z} = 0, \tag{4.21}$$

which is the perfectly reflecting case and

$$\varepsilon = 1 \rightarrow \frac{\partial B_y}{\partial z} = \frac{i\omega}{v_A}B_{1y}, \tag{4.22}$$

which is the perfectly transparent case.

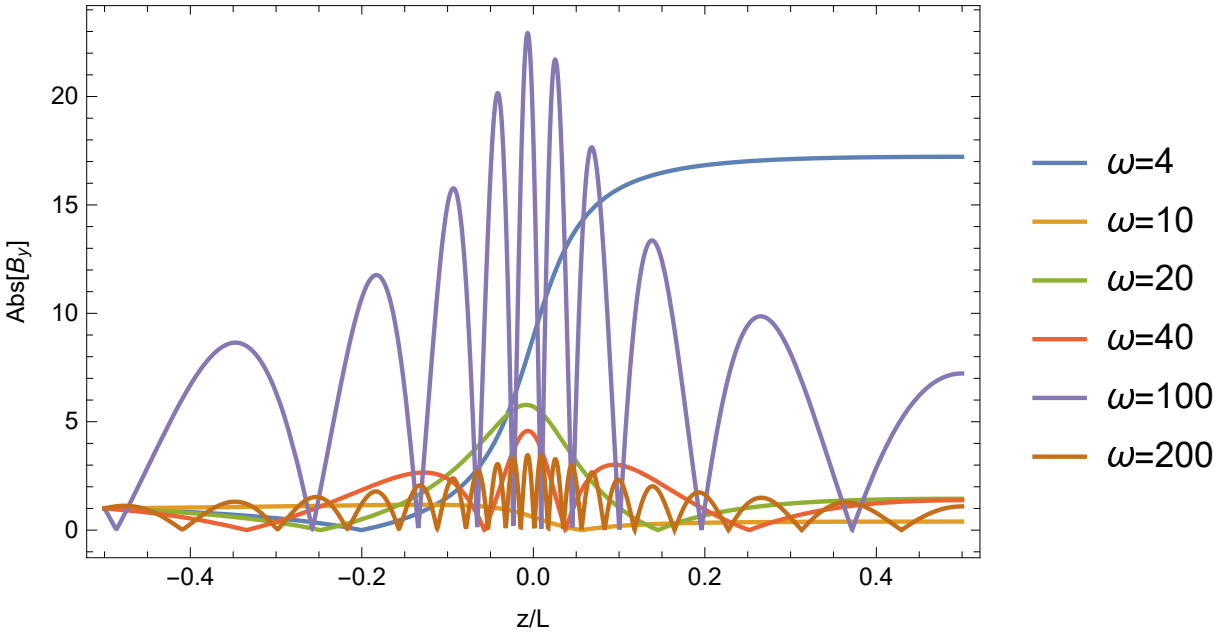

(a) Saha

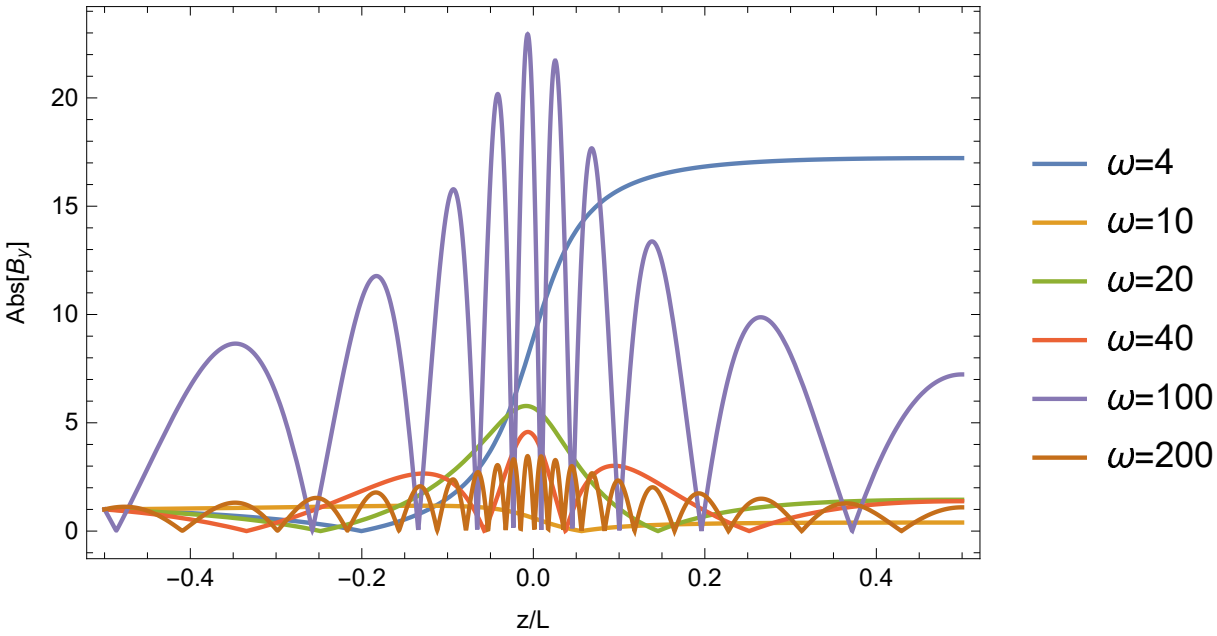

(b) Heinzel

Figure 21: *Absolute value of the magnetic field perturbation along the thread in the case of propagating waves that are driven at the left end. Results in the case of Saha and Heinzel profiles. Arbitrary units are used so that* $|B_y| = 1$ *at* $z/L = -1/2$.

4.2.1 Solutions

We have plotted the results of six frequencies of reference. The plots are displayed in Figure 21 for the perfectly reflected case ($\varepsilon = 0$). We have plotted the magnetic field perturbation for $\overline{\omega} = 4, 10, 20, 40, 100, 200$.

In the plots we can see that for a given frequency the absolute values of the magnetic field perturbation obtained for both methods are almost the same. We see that the shape of the functions is related to the frequency. The perturbations corresponding to the lowest frequencies display less oscillations that those corresponding to the highest frequencies. For example, the function of $\overline{\omega} = 4$ has no peak, whereas the function related to $\overline{\omega} = 200$ has 17 peaks, and these peaks tend to be narrower when they are close to the centre of the thread. To understand these results we have to take into account that for an Alfvén wave, the higher the frequency, the shorter the wavelength. This explains why the results for high frequencies display more oscillations that for those for low frequencies. In addition, in an Alfvén wave the wavelength is also proportional to the Alfvén speed. At the centre of the thread, the Alfvén speed is smaller than at the ends of the thread because the density is larger at the centre. Hence, the variation of the Alfvén speed along the thread explains why the local wavelengths of the perturbations are shorter around the thread centre.

We have solved Equation (3.34) using the values of 0,0.5 and 1 for ε for both methods and we have plotted the absolute value of the magnetic field perturbation. The results are in Figure 22. For this calculation we have assumed $\overline{\omega} = 4$.

For these plots we see that the two methods give almost the same results, which is consistent with the other results of the study. After analysing the results we see that the function with the highest amplitude corresponds to the case of $\varepsilon = 0$, whereas the case with the lowest amplitude is consistent $\varepsilon = 1$. This result implies that when the transparency of the thread is bigger, the amplitude of the magnetic field perturbation will be lower.

We solve again the equation but with $\overline{\omega} = 94$. The results are in Figure 23.

In these plots we see that is the case of $\varepsilon = 1$ the one that has a higher amplitude for the magnetic field, whereas the case of $\varepsilon = 0$ is the one that has the lowest amplitude. This observation is interesting because the relative amplitude of the solutions has changed and now it is the case with total reflection the one with the maximum amplitude. To understand this result, we note that $\overline{\omega} = 94$ is a frequency value very close to an eigenvalue of the standing case, while the value $\overline{\omega} = 4$ is far from any eigenvalue. The relative amplitude of the solutions in the case $\overline{\omega} = 94$ suggests that part of the driven energy may go to the excitation of the standing mode with that frequency. This is explained in more detail in the following section.

4.2.2 Energy flux

Once we have analysed the effect of parameters on the magnetic field perturbation, we can compute the dependence of the driven energy flux with the frequency. We have calculated the energy flux driven at the left end of the thread. The results are represented in Figure 24.

The plots are in logarithmic scale to make the change of the values more visible. The energy flux has a similar behaviour for all the values of ε taken, being an initial large parabola,then a peak followed by oscillations with less amplitude. The main difference between the three values is the amplitude of the flux, being the case of $\varepsilon = 0$ the one with the highest oscillations, whereas the case of $\varepsilon = 1$ has a small amplitude change. In the case of $\varepsilon = 0$ the minimums of the flux tend to be higher when the frequency considered is higher. Comparing the Saha and Heinzel

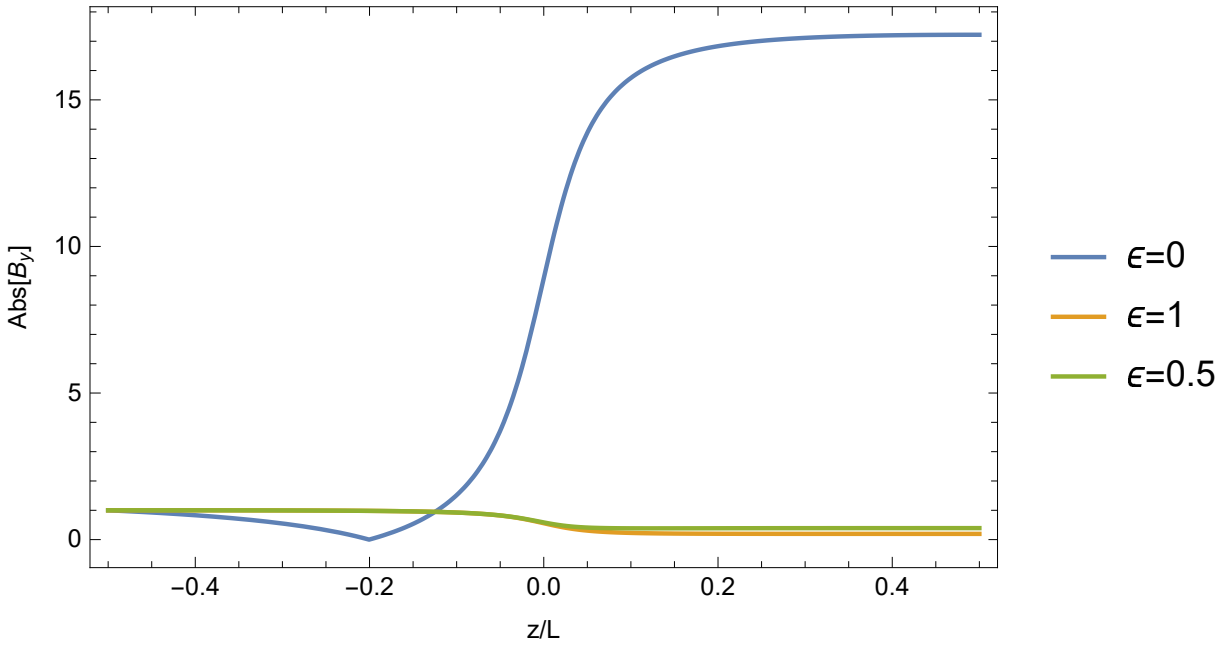

(a) Saha

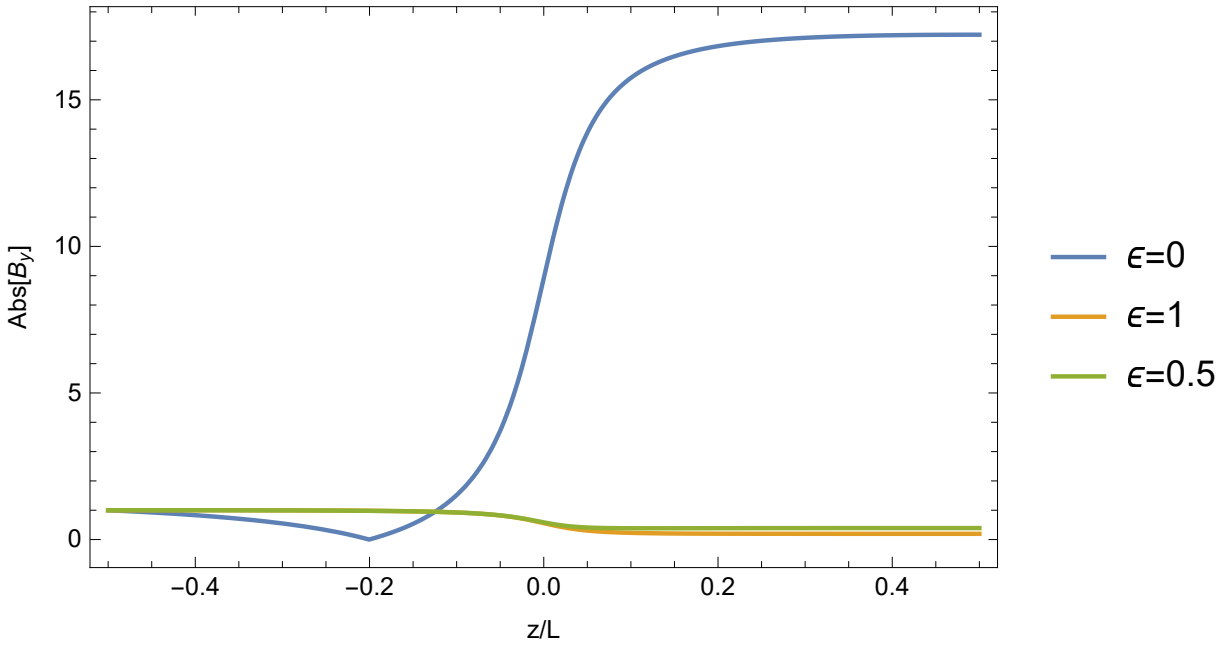

(b) Heinzel

Figure 22: *Magnetic field perturbation for the propagating modes in Saha and Heinzel profiles for three values of* ε *for* $\overline{\omega} = 4$.

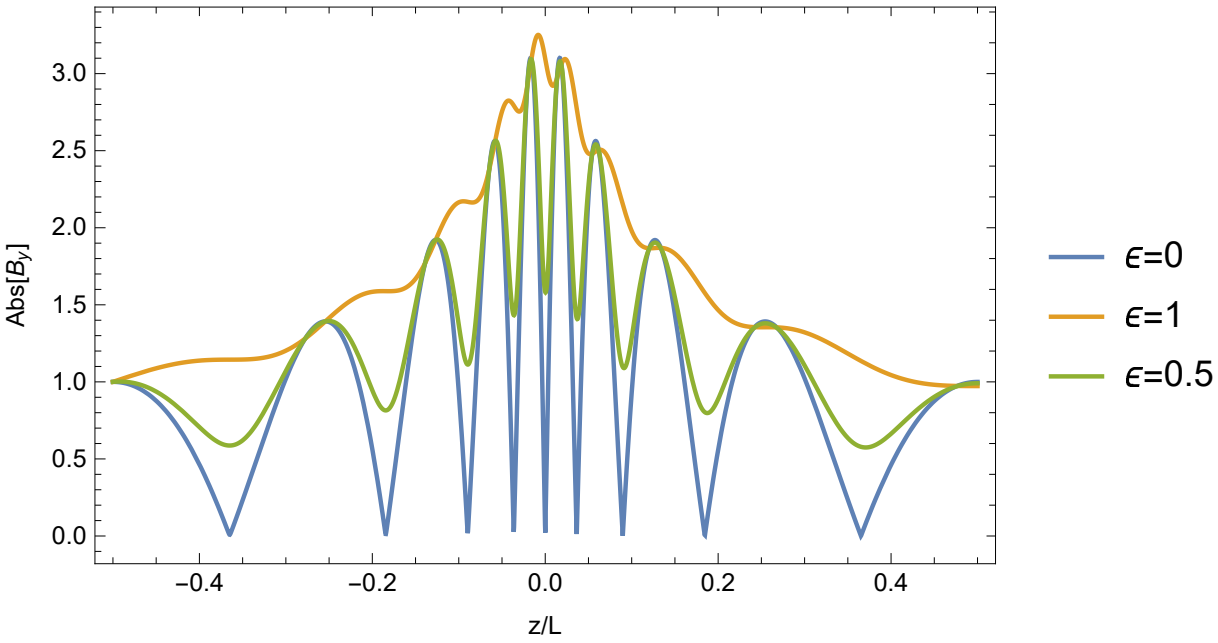

(a) Saha

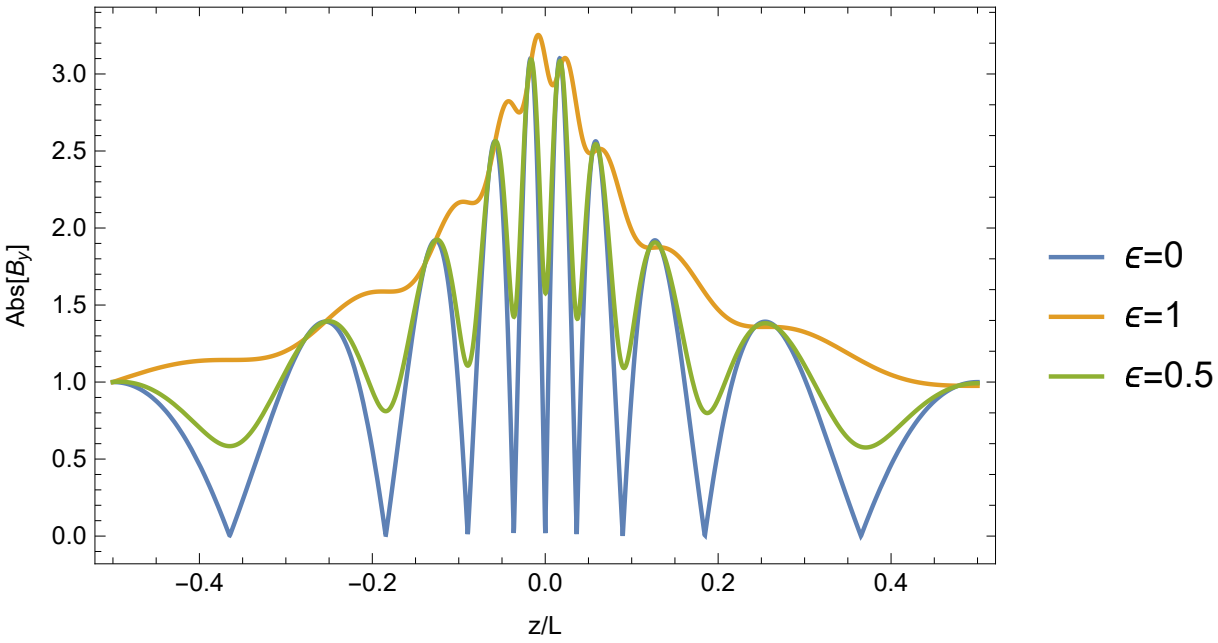

(b) Heinzel

Figure 23: *Same as Figure 22 but for* $\varpi = 94$.

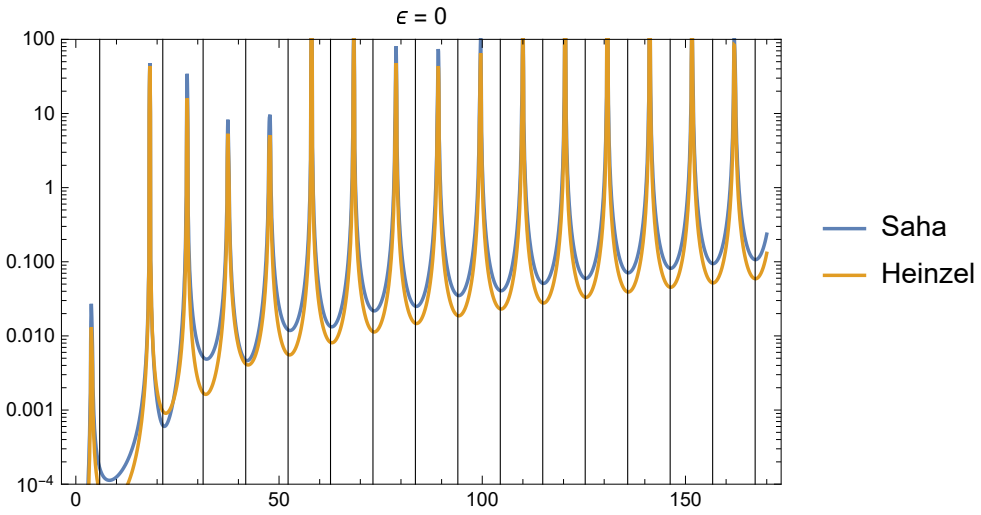

(a) $\varepsilon = 0$

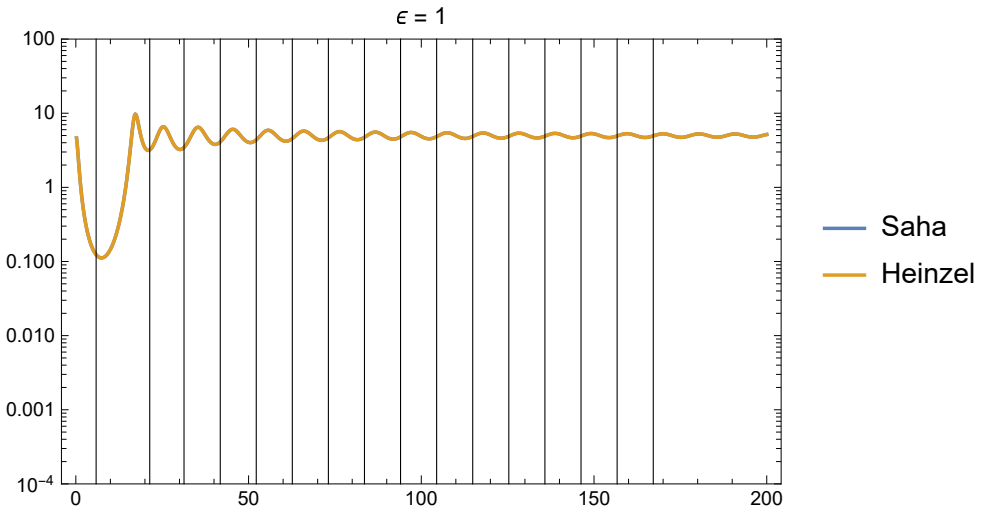

(b) $\varepsilon = 1$

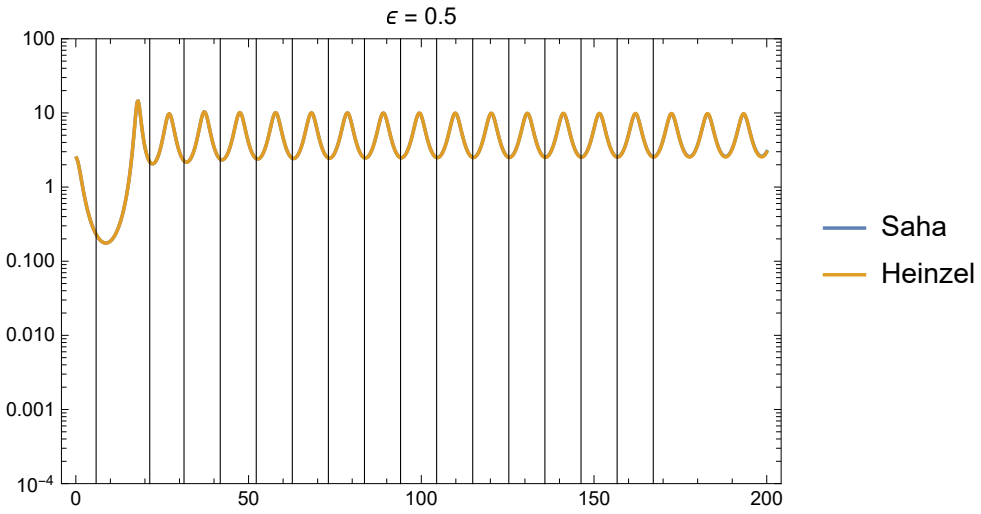

(c) $\varepsilon = 0.5$

Figure 24: Energy flux in arbitrary units for Saha and Heinzel profiles.

methods, the difference between them are more visible in the $\varepsilon = 0$ case, where in almost all the range of frequencies the Saha method gives a higher value of the energy flux than the Heinzel method. In the other cases the difference between the two methods is negligible.

In the plots he have represented with vertical lines the eigenfrequencies from the standing modes case. We can see that for all cases considered there is a correspondence between the minimums of the energy flux and the eigenfrequencies. This result suggests the existence of a resonance in the thread. When the driver frequency matches an eigenfrequency of the system, the net energy flux is minimum. This is consistent with the fact that for a standing wave, represented as the superposition of two waves propagating in opposite directions, the net flux of energy is zero.

4.2.3 Reflectivity, transmissivity and absorption

We define the reflectivity $\mathcal{R}$ and transmissivity $\mathcal{T}$ coefficients which physically represent the fractions of the driven wave energy that are reflected and transmitted respectively [37]. We define the incident, reflected and transmitted fluxes as

$$\langle \pi \rangle_{inc.} = \langle \pi \rangle^{\uparrow}, \quad at \quad z = -L/2, \tag{4.23}$$

$$\langle \pi \rangle_{ref.} = \langle \pi \rangle^{\downarrow}, \quad at \quad z = -L/2, \tag{4.24}$$

$$\langle \pi \rangle_{tra.} = \langle \pi \rangle, \quad at \quad z = L/2, \tag{4.25}$$

with these fluxes the coefficients are computed as

$$\mathcal{R} = -\frac{\langle \pi \rangle_{ref.}}{\langle \pi \rangle_{inc.}}, \quad \mathcal{T} = \frac{\langle \pi \rangle_{tra.}}{\langle \pi \rangle_{inc.}}. \tag{4.26}$$

Using the energy conservation, we can compute the absorption, which is the fraction of the incident wave of energy that is dissipated or absorbed in the plasma because of dissipation. This absorption is defined as

$$\mathcal{A} = 1 - \mathcal{R} - \mathcal{T}. \tag{4.27}$$

We calculate the reflectivity , transmissivity and absorption for the frequency ranging from $\overline{\omega} = 0.2$ to $\overline{\omega} = 1190.2$. The results are in the Figures (25a) to (25c).

Analysing the plots, we see that the transmissivity is zero in the case with $\varepsilon = 0$, which is related to the definition of this parameter. The absorption increases its value when the frequency of wave increases, whereas the reflectivity and the transmissivity decreases. This is consistent with the fact that the efficiency of the dissipation mechanisms increases with the wave frequency. Comparing the results of the three different values of ε, we see that the absorption is larger for the $\varepsilon = 0$ case, decreasing the maximum value for larger values of ε. For $\varepsilon = 0$ energy can not scape through the right end of the thread, so that there is more energy available in the system to be dissipated. For the case $\varepsilon = 0.5$ the reflectivity has a much lower value than the transmissivity for almost all the frequency range calculated. In this case the maximum value of the transmissivity reaches a lower value than the case of $\varepsilon = 1$, where it reaches a value of 1 approximately. Comparing the Saha and Heinzel profiles for all the cases, we see that the Saha profile gives a higher value for the absorption pointing out that wave dissipation is more efficient for the Saha profile than for the Heinzel profile. In the case of the reflectivity and transmissivity is the Heinzel profile the one that has higher values.

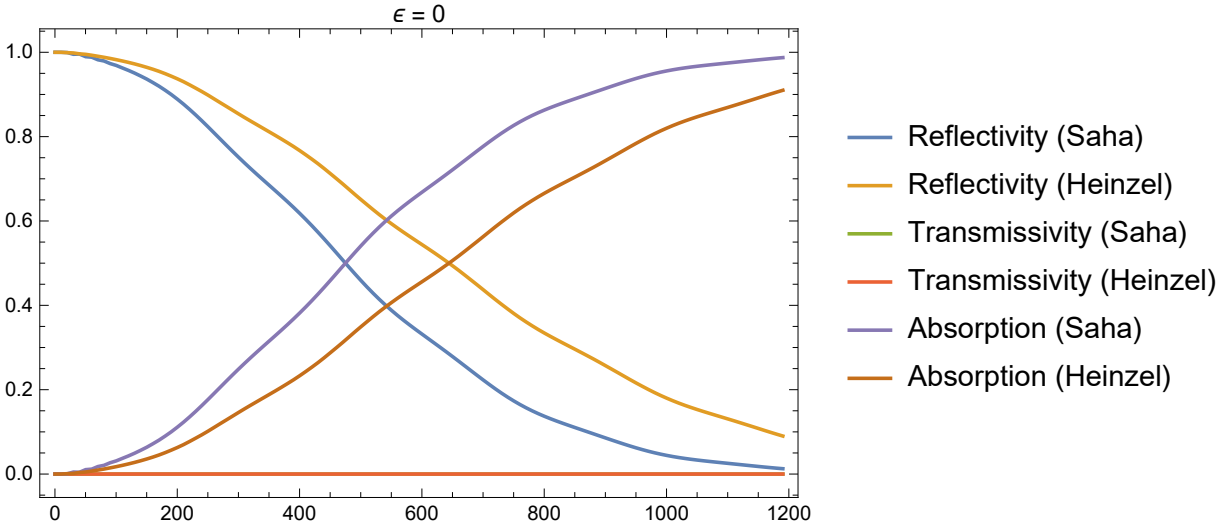

(a) $\varepsilon = 0$

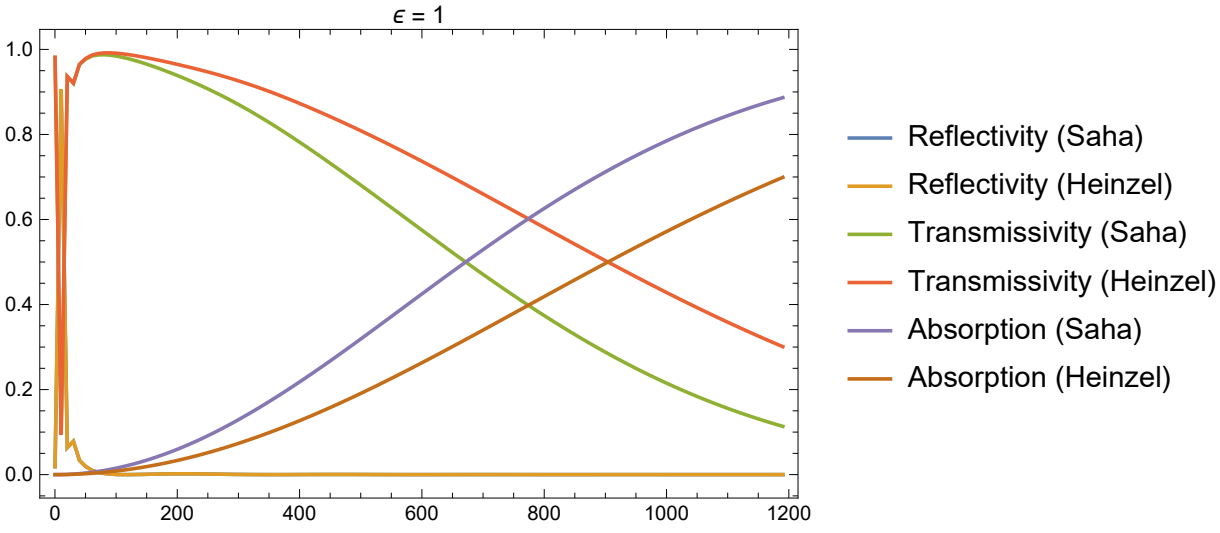

(b) $\varepsilon = 1$

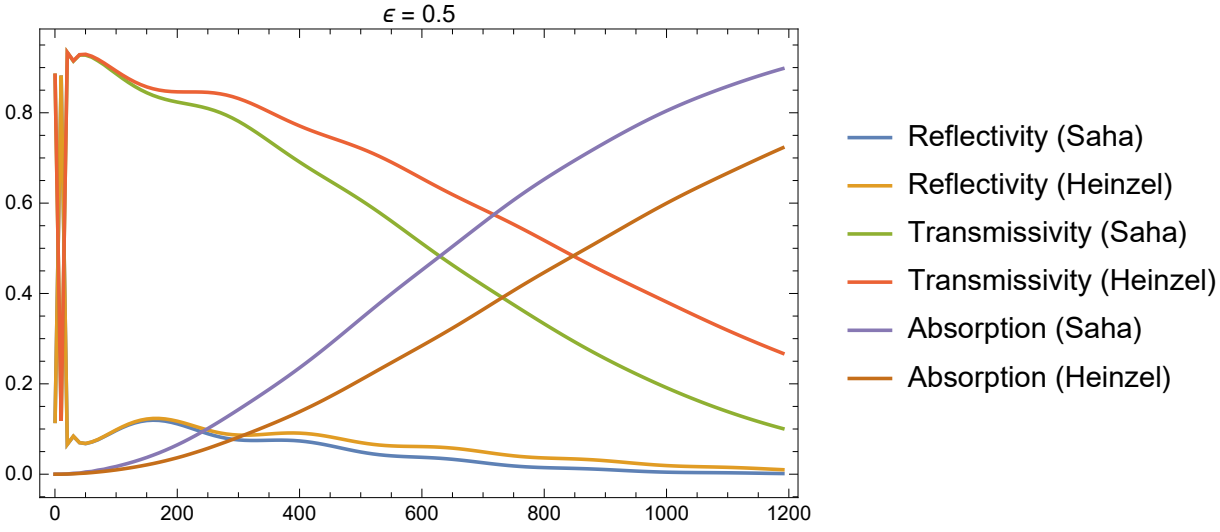

(c) $\varepsilon = 0.5$

Figure 25: Reflectivity , transmissivity and absorption for Saha and Heinzel methods.

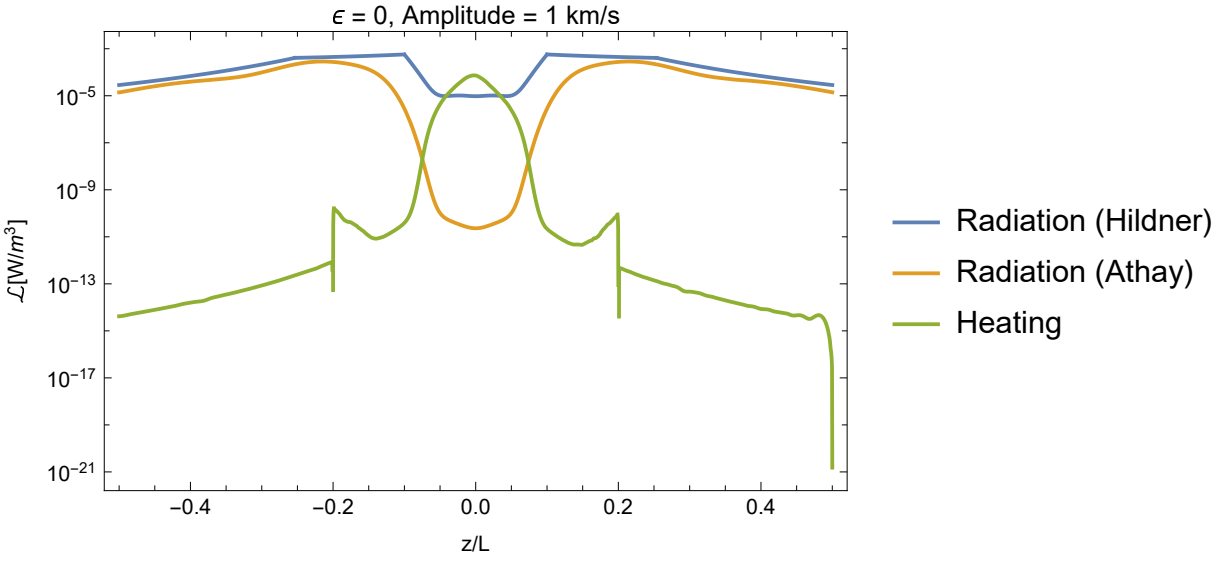

(a) Saha

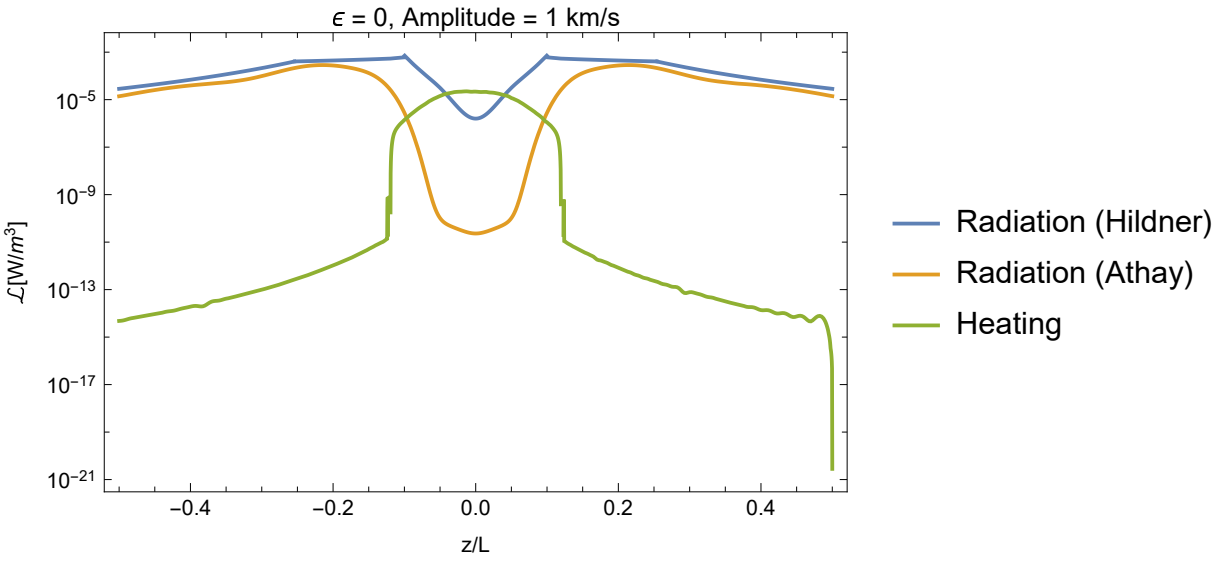

(b) Heinzel

Figure 26: *Energy balance in the Saha and Heinzel profiles for a broadband driver.*

4.2.4 Energy balance for a broadband driver

The next step is to compute the energy balance, which is done in the same way as for the standing mode case. Using Equation (4.9) for the heating function and Equations (4.10) and (4.11) for the Hildner and Athay cooling, respectively. For this estimations, instead of considering a single frequency, we assume that the driver excites a broadband spectrum in order to mimic the excitation of waves that may happen in the photosphere where the magnetic field lines are anchored. The heating functions have been calculated for all the driven frequencies in the considered range and the results has been added together assuming a constant velocity amplitude of 1 $\mathrm{km\,s^{-1}}$ at the left end of the thread (i.e., the driver location). The energy balance for the Saha and Heinzel methods are in Figure 26.

In the plots the cooling functions are the same as those shown in the standing modes case. For the heating part, the shape of the function is similar to the standing modes case, having an increase at the centre of the thread and much lower value in the ends. Comparing the heating and cooling functions in both cases, we see that the heating has a higher value at the centre of

the thread than both Athay and Hildner cooling functions. The main difference between Saha and Heinzel profiles is that for the Saha profile the heating function has a narrower peak where has a higher value than the cooling functions, whereas in the Heinzel profile it has a wider peak. This difference could be related with the ionisation fraction, because this region has the same extend that the partially ionised region for both methods.

If we analyse the heating function using the Ohm and ambipolar diffusion, we conclude that the ambipolar diffusion is dominant at the centre of the thread, whereas in the evacuated part the Ohm diffusion is the only acting mechanism, since the ambipolar diffusion is zero in a fully ionised plasma.

The next step is to calculate the integrated heating rate and comparing it with the radiative loses integrated along the thread. This calculation is made by integrating the functions of heating along all the thread first, and then doing the same calculation for the central part only, which corresponds to $-0.2 < z/L < 0.2$. This calculation is compared with the integrated cooling functions for both Hildner and Athay cases. This is, we perform the ratio of the integrated heating to the integrated cooling. We do the calculations in the case $\varepsilon = 0$. The results are presented in percentages in Table 4.

Ratio %	**Hildner all**	**Hildner central**	**Athay all**	**Athay central**
Saha	1.4403	2.79749	3.71165	12.1266
Heinzel	1.09961	2.05907	2.95133	9.65846

Table 4: Ratio (%) of integrated heating to radiative loses for $\varepsilon = 0$.

The results indicate that only a small fraction of the total radiative losses is compensated by wave heating. The Saha profiles provide slightly larger values of the heating to cooling ratio than the Heinzel profiles. Again, this points out that wave dissipation is a bit more efficient when the profiles in the Saha case are used. Also, the ratio heating to cooling is larger when the Athay cooling function is used, compared with the result of the Hildner cooling function. The reason is that, as explained before, the radiation provided by the Athay function is much lower in the cool part of the thread.

The situation improves when we only consider the central, dense part of the thread. The values of the heating to cooling ratio for the Hildner cooling function are still unimportant, but in the case of the Athay cooling function we find that wave heating can compensate for about 10 % of radiative losses. This result agrees with the previous calculation of [36], who found that in a more simplified slab model, Alfvén wave heating could compensate for a similar fraction of radiation losses.

5 Conclusions, discussion and future work

The purpose of this work has been studying the impact of Alfvén wave heating in the energy balance in solar prominence threads. We have started by considering a simplified 1D model of a very thin thread made of a single magnetic field line. A Lorentzian profile for the density has adopted. To obtain the temperature and ionisation profiles, we have used two cases, one considering the Saha equation under the LTE assumption and another one considering results from non-LTE radiative transfer computations (Heinzel profiles). Subsequently, we have computed the profiles of the dissipation coefficients η and η_A.

To study Alfvén waves, we have used the linearised MHD equations for a partially ionised plasma in the single-fluid approximation. We have derived the governing equations for Alfvén waves in the stationary state, for both standing and propagating modes.

First, we have solved the eigenvalue problem of the standing modes and have computed their complex eigenfrequencies and eigenfunctions. We have obtained that the standing modes are weakly damped in our model, unless very high harmonics are considered. Regarding the energy balance, we have compared the wave energy dissipated along the thread with the radiation losses represented by either the Hildner or the Athay cooling functions. We have obtained that the dissipation of the standing modes is largely inefficient except in the densest part of the thread, where the wave heating can compensate cooling in the Athay case. The region where wave heating is important is wider for the Saha profiles than for the Heinzel ones. The reason is in the shape and values of the dissipation coefficients corresponding to each case.

Then, we have turned to propagating waves. We have assumed the presence of a driver at the left end of the thread that excites a broadband spectrum of the waves. The computations of the energy flux at the driver location shows evidence that standing modes are excited in the thread when the driver frequency matches an eigenfrequency. In addition, we have considered at the right end different boundary conditions representing total reflection, partial reflection, and total transmission. We have obtained that the absorption of wave energy in the thread gets more efficient as the driver frequency increases. The case in which total reflection is imposed is the one that gives larger absorption rates, since wave energy is unable to leave the system through the right boundary. The computations of the heating rates reveal that heating is unimportant in the evacuated (corona) part of the thread, while in the dense (prominence) part heating can compensate for about 10 % of radiative losses. As in the standing case, the heating rates obtained for the Saha profiles are larger than those of the Heinzel profiles.

In the work [36] they considered a slab model for the density, which consisted in having a uniform density in three regions, being the central part the prominence and the sides the solar corona. They only studied propagating modes. They saw the existence of resonances in the absorption rate when the driver frequency matches an eigenfrequency of the slab. They concluded too that the absorption for low frequencies is almost negligible, as we have seen in our study. Efficient absorption take place for high frequencies. For the energy balance part, they computed too that the heating function could compensate around the 10 % of the cooling functions. In this work we have used a continuous density profile, so there is a transition region instead of having an sharp change of density and we do not find the absorption resonances discussed in the previous work. Remnant of resonances are, however, seen in the energy flux.

In the future, we plan to extend this investigation in several ways. Some of the assumptions considered here could be relaxed. For instance, we can use a more realistic 2D and 3D models instead of the simplified 1D model used here. In addition, we can consider a purely numerical approach instead of the semi-analytic method used here. This will enable us to investigate non-linear effects and to study the temporal evolution beyond the stationary case investigated here.

References

[1] Iñigo Arregui, Ramón Oliver, and José Luis Ballester. Prominence oscillations. *Living Reviews in Solar Physics*, 9(1):2, 2012.

[2] Markus Aschwanden. *Physics of the solar corona: an introduction with problems and solutions*. Springer Science & Business Media, 2006.

[3] RG Athay. Radiation loss rates in lyman-alpha for solar conditions. *The Astrophysical Journal*, 308:975–981, 1986.

[4] José Luis Ballester. Magnetism and dynamics of prominences: Mhd waves. In *Solar prominences*, pages 259–296. Springer, 2015.

[5] H Balthasar, M Knölker, E Wiehr, and G Stellmacher. Evidence for quasi-periodic doppler motions in solar prominences. *Astronomy and Astrophysics*, 163:343–346, 1986.

[6] S Barceló, M Carbonell, and JL Ballester. Time damping of non-adiabatic magnetohydrodynamic waves in a partially ionised prominence medium: Effect of a background flow. *Astronomy & Astrophysics*, 525:A60, 2011.

[7] VS Bashkirtsev, NI Kobanov, and GP Mashnich. The observations of 80-min oscillations in the quiescent prominences. In *International Astronomical Union Colloquium*, volume 66, pages 443–445. Cambridge University Press, 1983.

[8] VS Bashkirtsev and GP Mashnich. Oscillatory processes in prominences. *Solar physics*, 91(1):93–101, 1984.

[9] Thomas E Berger, Richard A Shine, Gregory L Slater, Theodore D Tarbell, Takenori J Okamoto, Kiyoshi Ichimoto, Yukio Katsukawa, Yoshinori Suematsu, Saku Tsuneta, Bruce W Lites, et al. Hinode sot observations of solar quiescent prominence dynamics. *The Astrophysical Journal Letters*, 676(1):L89, 2008.

[10] Cornelius De Jager. Structure and dynamics of the solar atmosphere. In *Astrophyysics III: The Solar System/Astrophysik III: Das Sonnensystem*, pages 80–362. Springer, 1959.

[11] PM Edwin and B Roberts. Wave propagation in a magnetic cylinder. *Solar Physics*, 88(1-2):179–191, 1983.

[12] John Warren Harvey. Magnetic fields associated with solar active-region prominences. *PhDT*, 1969.

[13] P Heinzel and U Anzer. On the fine structure of solar filaments. *The Astrophysical Journal Letters*, 643(1):L65, 2006.

[14] P Heinzel, S Gunár, and U Anzer. Fast approximate radiative transfer method for visualizing the fine structure of prominences in the hydrogen hα line. *Astronomy & Astrophysics*, 579:A16, 2015.

[15] E Hildner. The formation of solar quiescent prominences by condensation. *Solar Physics*, 35(1):123–136, 1974.

[16] Andrew Hillier, RJ Morton, and Robert Erdélyi. A statistical study of transverse oscillations in a quiescent prominence. *The Astrophysical Journal Letters*, 779(2):L16, 2013.

[17] PS Joarder, VM Nakariakov, and B Roberts. Oscillations in prominence fine-structures. *Solar Physics*, 173(1):81–101, 1997.

[18] PS Joarder and B Roberts. The modes of oscillation of a prominence. ii-the slab with transverse magnetic field. *Astronomy and Astrophysics*, 261:625–632, 1992.

[19] Max Kuperus and Einar Tandberg-Hanssen. The nature of quiescent solar prominences. *Solar Physics*, 2(1):39–48, 1967.

[20] DONALD A Landman, STEPHEN J Edberg, and C DAVID Laney. Measurements of h-beta, he d3, and ca/+/8542-a line emission in quiescent prominences. *The Astrophysical Journal*, 218:888–897, 1977.

[21] Leping Li and Jun Zhang. The evolution of barbs of a polar crown filament observed by sdo. *Solar Physics*, 282(1):147–174, 2013.

[22] Yong Lin. Filament thread-like structures and their small-amplitude oscillations. *Space science reviews*, 158(2-4):237–266, 2011.

[23] Yong Lin, O Engvold, LHM Rouppe Van der Voort, and Michiel van Noort. Evidence of traveling waves in filament threads. *Solar Physics*, 246(1):65–72, 2007.

[24] Yong Lin, OddbjØrn Engvold, Luc Rouppe van der Voort, Jun Elin Wiik, and Thomas E Berger. Thin threads of solar filaments. *Solar Physics*, 226(2):239–254, 2005.

[25] Yong Lin, OddbjØ rn Engvold, and Jun Elin Wiik. Counterstreaming in a large polar crown filament. *Solar Physics*, 216(1-2):109–120, 2003.

[26] Bruce W Lites, M Kubo, T Berger, Z Frank, R Shine, T Tarbell, TJ Okamoto, K Otsuji, et al. Emergence of helical flux and the formation of an active region filament channel. *The Astrophysical Journal*, 718(1):474, 2010.

[27] R Molowny-Horas, E Wiehr, H Balthasar, R Oliver, and JL Ballester. Prominence doppler oscillations. *joso*, pages 126–127, 1999.

[28] Z Ning, W Cao, and PR Goode. Behavior of the spines in a quiescent prominence observed by hinode/sot. *The Astrophysical Journal*, 707(2):1124, 2009.

[29] R Oliver, JL Ballester, AW Hood, and ER Priest. Oscillations of a quiescent solar prominence embedded in a hot corona. *The Astrophysical Journal*, 409:809–821, 1993.

[30] Ramon Oliver. Prominence oscillations: observations and theory. In *Magnetic Fields and Solar Processes*, volume 448, page 425, 1999.

[31] Susanna Parenti. Solar prominences: observations. *Living Reviews in Solar Physics*, 11(1):1, 2014.

[32] Eric Priest. *Magnetohydrodynamics of the Sun*. Cambridge University Press, 2014.

[33] Stephane Regnier, J Solomon, and Jean-Claude Vial. Oscillations in an active region filament: Observations and comparison with mhd waves. *Astronomy & Astrophysics*, 376(1):292–301, 2001.

[34] R Soler, Marcel Goossens, and JL Ballester. Prominence seismology using the period ratio of transverse thread oscillations. *Astronomy & Astrophysics*, 575:A123, 2015.

[35] R Soler, R Oliver, and JL Ballester. Magnetohydrodynamic waves in a partially ionized filament thread. *The Astrophysical Journal*, 699(2):1553, 2009.

[36] Roberto Soler, Jaume Terradas, Ramon Oliver, and Jose Luis Ballester. The role of alfvén wave heating in solar prominences. *Astronomy & Astrophysics*, 592:A28, 2016.

[37] Roberto Soler, Jaume Terradas, Ramón Oliver, and José Luis Ballester. Energy transport and heating by torsional alfvén waves propagating from the photosphere to the corona in the quiet sun. *The Astrophysical Journal*, 871(1):3, 2019.

[38] E Wiehr, G Stellmacher, and H Balthasar. Oscillations of the hα emission in solar prominences. *Solar physics*, 94(2):285–288, 1984.

[39] Zhang Yi and Oddbjørn Engvold. Vertical velocities and oscillations in quiescent filaments. *Solar physics*, 134(2):275–286, 1991.

[40] Zhang Yi, Oddbjorn Engvold, and Stephen L Keil. Structure and oscillations in quiescent filaments from observations in he i 10830 a. *Solar physics*, 132:63–80, 1991.